A wireless and battery-less implant for multimodal closed-loop neuromodulation in small animals

Wei Ouyang [1,22], Wei Lu[1,22], Yamin Zhang[1,22], Yiming Liu[2], Jong Uk Kim[1,3], Haixu Shen[4], Yunyun Wu[1], Haiwen Luan[1], Keith Kilner [5], Stephen P. Lee[1,5], Yinsheng Lu [4], Yiyuan Yang[6], Jin Wang[4], Yongjoon Yu[5], Amy J. Wegener[7,8], Justin A. Moreno[7,8,9], Zhaoqian Xie[4,6,10], Yixin Wu [4], Sang Min Won [11], Kyeongha Kwon [12], Changsheng Wu[1], Wubin Bai [1,4,13], Hexia Guo [4], Tzu-li Liu[6], Hedan Bai[1], Giuditta Monti[14], Jason Zhu[15,16], Surabhi R. Madhvapathy[4], Jacob Trueb [1], Maria Stanslaski[5], Elizabeth M. Higbee-Dempsey [17], Iwona Stepien[17], Nayereh Ghoreishi-Haack[17], Chad R. Haney [18], Tae-il Kim [3,19], Yonggang Huang [1,4,6,10], Roozbeh Ghaffari [1,5], Anthony R. Banks[1,5], Thomas C. Jhou [20] ✉, Cameron H. Good [1,5,7,8] ✉ & John A. Rogers [1,4,6,14,16,21] ✉

Fully implantable wireless systems for the recording and modulation of neural circuits that do not require physical tethers or batteries allow for studies that demand the use of unconstrained and freely behaving animals in isolation or in social groups. Moreover, feedback-control algorithms that can be executed within such devices without the need for remote computing eliminate virtual tethers and any associated latencies. Here we report a wireless and battery-less technology of this type, implanted subdermally along the back of freely moving small animals, for the autonomous recording of electroencephalograms, electromyograms and body temperature, and for closed-loop neuromodulation via optogenetics and pharmacology. The device incorporates a system-on-a-chip with Bluetooth Low Energy for data transmission and a compressed deep-learning module for autonomous operation, that offers neurorecording capabilities matching those of gold-standard wired systems. We also show the use of the implant in studies of sleep–wake regulation and for the programmable closed-loop pharmacological suppression of epileptic seizures via feedback from electroencephalography. The technology can support a broader range of applications in neuroscience and in biomedical research with small animals.

Recordings of neurophysiological activity, typically in the form of electroencephalography (EEG) and electromyography (EMG), represent well-established essential sources of information for quantitative investigations of neural processes and for the development of neurological medical systems[1–4]. Research in learning and memory and in other cognitive processes, as well as neurodevelopmental and neurodegenerative disorders, relies critically on neurophysiological measurements[5–7]. Studies of sleep–wake regulation, typically exploiting EEG and EMG, are especially active areas of research, as the underlying mechanisms of sleep remain mysterious despite its enormous clinical

and biological importance[8,9]. Traditional neurophysiological recording systems for animal models use electrodes that attach to the skull (EEG), neck muscles (EMG) or other regions of interest and that, in turn, connect via physical tethers to external recording equipment[2]. These systems can be effective, but they substantially restrict movement and can alter natural patterns of behaviour, especially in small animals such as rodents, birds and fish[4]. In addition, the tethers prevent certain kinds of study, such as those involving social interactions or the exploration of naturalistic three-dimensional environments. Also, they introduce stress-related artefacts that disrupt sleep–wake regulation and other cognitive processes[4,10,11].

Neurophysiological recording technologies together with approaches for neuromodulation can be used to obtain fundamental insights into neural circuit processes and dynamics[12–14]. Compared with conventional electrical-stimulation methods, neuromodulation by optogenetic and pharmacological means is of broad and growing interest to the neuroscience community because they offer cellular specificity with well-defined mechanisms[15]. From the standpoint of the enabling neurotechnology hardware, the associated engineering requirements increase the extent of physical tethering of the animals through a need for additional fibre-optic cables that couple to external light sources or for tubing that connects to external pump systems[12,13]. These interfaces and their associated percutaneous connectors cause tissue damage and are prone to entanglement, thereby limiting the reliability, duration and types of experimental study; they also create high levels of stress in the animals, with potentially confounding effects on experimental outcomes.

Existing wireless technologies for neurorecording and/or neuromodulation typically rely on headstages or backpacks to house the electronics and the battery (Supplementary Table 1). The bulk, weight and rigidity of these components, along with the associated open interfaces to the brain, induce physiological and psychological stresses that can strongly alter behaviours. The exposed hardware leads to clawing and biting among groups of animals, thereby preventing studies of social interactions. Furthermore, battery-powered devices have limited operation time, particularly those that offer capabilities in neuromodulation, thereby preventing chronic studies (Supplementary Table 1). Wireless, fully implantable, battery-free systems that offer chronic stability and broad multimodal functionality represent a universal ideal across nearly all areas of neuroscience and biomedical research involving freely moving animals. Although recent publications report systems with some of these features for physiological monitoring (for example, oximetry and photometry) and separately for optogenetic and/or pharmacological neuromodulation (Supplementary Table 2), wirelessly powered, high-fidelity capabilities in neurorecording in a single system that also offers multimodal options in neuromodulation exceed the features of any system reported in the literature. Here we introduce such a technology, built using readily available commercial components[4], to facilitate the possibility for broad dissemination across the neuroscience research community.

Beyond uses in research, advanced closed-loop systems that offer real-time feedback control of neuromodulation based on data from neurorecording offer considerable promise in neurorehabilitation and therapeutic management of neurological conditions, such as movement disorders, depression and drug addiction[16,17]. In particular, such capabilities are critical for monitoring and timely mitigation of abrupt life-threatening conditions such as epilepsy and drug overdose. At the heart of such autonomous systems are signal processing and decision-making algorithms that recognize and quantify responses to adjust stimulation parameters accordingly. Algorithms directly embedded in the device are attractive in this context by eliminating concerns about latency, privacy and security associated with remote computing in the event of disrupted connectivity and data breach. Conventional hardware-implemented algorithms, such as feature thresholding or linear discriminant analysis, rely on domain-specific pipelines, with

substantial inter-subject variability[18,19]. Neurosignal pattern recognition by deep learning, despite the necessity for interpretability for clinical translation still under debate[20], represents a paradigm of growing interest because of the generalizability to different subjects, domain independence and demonstrated high accuracy[21–24]. Via optimized codes, deployment of deep learning models is possible even with constrained central processing unit (CPU) and memory resources on microcontrollers at low power consumption[25].

Here we report a wireless, battery-free and fully implantable system capable of supporting artificial intelligence (AI) algorithms, for autonomous closed-loop neurorecording and neuromodulation. The advances reported here support the following features: (1) high-performance recording of EEG, EMG and body temperature; (2) programmable neuromodulation by optogenetics and pharmacology; (3) battery-free operation powered by magnetic inductive coupling at a standard near-field communication (NFC) frequency of 13.56 MHz, with probes, electronics and filters that eliminate electromagnetic interference; (4) wireless and continuous data streaming to a graphical user interface (GUI); (5) an AI-enabled autonomous mode for closed-loop operation; and (6) a lightweight, flexible and miniaturized device that mounts subdermally on the back of small animal models and that distributes its mass across the body of the animal, with minimal burden on mobility.

A rigorous set of benchmark tests against a state-of-the-art tethered setup for EEG recording established equivalency in operation across settings spanning baseline conditions to pharmacologically induced seizures. Additional results show capabilities for capturing small, millisecond-scale auditory-evoked potentials (AEPs). Long-term experiments illustrate stable function in freely moving animals over 6 weeks, including continuous tracking of sleep–wake cycles. Additional studies involve the use of embedded AI-controlled pharmacological suppression of epileptic seizures through feedback based on EEG patterns to highlight options in autonomous closed-loop neuromodulation. Taken together, this wireless and battery-free technology provides a broad range of options to support neuroscience research, all in freely moving and minimally perturbed animal models.

Results
Design concepts and system features

The system comprises wireless electronics and embedded algorithms that support neurorecording capabilities and options for augmentation with neuromodulation modalities of interest (optogenetic manipulation and/or drug delivery), all integrated in a single device and subdermally implanted along the back of the animal (Fig. 1a,b). The back subdermal design involves implantation procedures that are different from those for conventional systems, as illustrated in Supplementary Fig. 1. The EEG sensors for neurorecording include a pair of soft platinum black (PtBk)-coated gold electrodes mounted on cylindrical poly(dimethylsiloxane) (PDMS) posts that interface to the brain dura through burr holes in the skull. A separate pair of stainless-steel wires inserts into the neck muscles for EMG measurement. Neuromodulation hardware includes two microscale inorganic light-emitting diode (μ-ILED)-tipped probes that deliver light directly to deep brain tissue for bilateral optogenetic manipulation of the brain and two independently controlled drug delivery vehicles integrated into the device body. Thin stretchable serpentine interconnects travel subdermally along the back to connect the EEG, EMG and μ-ILED probes to a flexible printed circuit board (fPCB). The fPCB incorporates a Bluetooth Low Energy (BLE) system-on-a-chip (SoC) that (1) fetches data from analogue front-ends (AFEs) for EEG and EMG and from an embedded temperature sensor that monitors the peripheral body temperature, (2) modulates the operating parameters of the optogenetic probes, (3) controls the release of the drugs from the delivery vehicles and (4) performs wireless data communication to a GUI on a mobile device. The BLE SoC also embeds a compressed AI model and a deep learning inference framework tailored

for microcontrollers that support autonomous closed-loop operation on the basis of neurorecording and neuromodulation. The device wirelessly receives power via magnetic inductive coupling from an external antenna operating with NFC standards. Bioinert coatings of PDMS and parylene encapsulate the device as electrical and mechanical protection, with biofluid barrier properties that enable stable chronic operation. The completed device (Fig. 1c) features compliant mechanics, miniaturized dimensions and a total weight of approximately 1 g, with most of the mass evenly distributed across the back of the rat (typical weight of an adult animal is 250–350 g) and only 0.05 g on the head—a factor of more than 60 times less than that of traditional head-mounted wireless technologies[11,26,27].

The key defining characteristics, compared to previously reported technologies[26,28,29], are wireless, fully implantable, mechanically flexible and battery-free designs, with combined capabilities in multimodal, bidirectional, AI-driven closed-loop neurorecording and neuromodulation. The form factor and modes of operation eliminate physical constraints associated with tethered recording and powering cables, and without the bulk, size, weight and limited operating times associated with battery-powered alternatives. Rats implanted with these devices can move and interact freely in an open-field environment (Fig. 1d), with no quantifiable change in patterns of behaviour. Computed tomography (CT) imaging (Fig. 1e) collected 2 weeks after surgery indicates that the device components remain in their original positions throughout this period, with no signs of degradation in functionality or appearance. The fast-growing fascia layer fully encapsulates and stabilizes the device within 2 weeks (Supplementary Fig. 2), thereby preventing migration of the device in chronic implantation.

Design of the electronics

The exploded-view schematic illustration in Fig. 1f shows the detailed structure of the device, which consists of a top encapsulation layer of parylene (30 μm) and PDMS (1 mm), a components layer, a double-layer fPCB (Cu (18 μm): polyimide (PI, 75 μm): Cu (18 μm)) and a bottom encapsulation layer. A loop antenna tuned to 13.56 MHz (10 turns, trace width/space of 100 μm/100 μm, area of 16 mm × 16 mm) receives power via resonant magnetic inductive coupling to a double-loop primary antenna that encircles the testing cage (31 cm × 34 cm). An external setup (Supplementary Fig. 3) that incorporates a 13.56 MHz radio-frequency (RF) generator and an impedance-matching circuit serves as a source of RF power. This antennae pair forms a loosely coupled wireless power transfer system, designed to alleviate sensitivities to slight mismatches in antenna characteristics and to allow wireless power transfer coverage throughout the cage.

The block diagram in Fig. 1g describes the electrical architecture of the device. The alternating current (AC) voltage induced on the receiver antenna passes through a full-wave bridge rectifier, to yield a stable direct current (DC) voltage of 2.7 V through a low-dropout regulator. The output powers the system and charges an array of 6 supercapacitors (7.5 mF each) as a temporary source of power that supports operation in the event of insufficient harvesting from wireless transfer. The BLE SoC comprises a Cortex M4 CPU that reads data from the sensors and controls the stimulators via general purpose inputs/outputs (GPIOs), a BLE 5 module that transceives data in a continuous streaming mode, and an embedded convolutional neural network (CNN) model and inference framework executed by the CPU and memory (random access memory (RAM) and flash memory) for operation in an autonomous closed-loop mode. The GPIOs interface with the EEG and EMG AFEs by the serial peripheral interface (SPI) protocol, with the temperature sensor by the inter-integrated circuit (I2C) protocol, with the μ-ILED probes by an application timer module and with the drug delivery vehicles by bipolar junction transistor (BJT) switches. Supplementary Fig. 4 presents a detailed electrical schematic of the system. Physical connections between the fPCB and the μ-ILED probes involve copper traces in serpentine layouts. Interfaces

to the EEG and EMG electrodes involve serpentine interconnects with twisted-pair copper traces for cancelling electromagnetic interference (Supplementary Fig. 5)[30–32]. Two reservoirs above the NFC antenna allow independent release of drugs subcutaneously upon triggering of electrolysis pumping processes via BJT switches, described in detail subsequently.

The main challenge in recording low-noise, high-quality EEG and EMG with this system is in rejection of electromagnetic interference associated with the power line noise at 60 Hz, the Bluetooth communication at 2.45 GHz and the 13.56 MHz NFC field that powers the system and permeates the volume of the cage. Design considerations that enable effective cancellation include (1) twisted-pair serpentine interconnects and layouts that isolate the AFE circuit and the NFC antenna at the far two ends of the fPCB; (2) matched resistors and matched X2Y capacitors that form single-pole low-pass differential-mode and common-mode filters with the poles located at approximately 1.6 kHz and 0.3 MHz at the input stage of the AFEs, respectively; and (3) circuits that drive the EEG and EMG inputs via 10 MΩ resistors with the inverse of the gained common-mode signal to further cancel common-mode (RF, Bluetooth and power line) noise and to hold the input bias signal voltage to the mid-supply of the amplifier for linear operation. As shown in Fig. 1h, an instrumentation amplifier (IN-AMP) amplifies the EEG and EMG signals after high-pass (HP) filtering, followed by passing them through an anti-aliasing filter (AAF), further amplification with a programmable-gain amplifier (PGA), digitization by a sigma-delta analogue-to-digital converter (ΣΔ ADC), decimation to 256 Hz (with an alternative of 512 Hz) and SPI read by a GPIO of the BLE SoC. The frequency response of the measurement circuit is flat from 0.5 Hz to 80 Hz (Supplementary Note 1 and Fig. 6a), ensuring undistorted recording of EEG and EMG signals[33]. System noise, measured by shorting the EEG and EMG input leads of a device powered by NFC, yields a peak-to-peak voltage (V_{pp}) of 3 μV, which is comparable to that from the same device powered by a battery (Supplementary Fig. 6b).

Animal studies indicate that the received signal strength indicator (RSSI) of an implanted device is about −65 decibel milliwatts (dBm) at a distance of 1 m and about −75 to −80 dBm at a distance of 2 m. The receiver tablet typically collects data from a distance of 1 m. Benchtop tests by submerging a device in phosphate buffered saline (PBS) to yield these RSSI values and comparing packets sent by the device and those received by the app (Supplementary Note 2) reveal packet error rates of 0 at 1 m and 1×10^{-4} at 2 m (bit error rates of 0 at 1 m and 1.6×10^{-6} at 2 m) that are consistent with values reported in the literature[34], thereby ensuring high-fidelity data transfer with a sufficient safety margin. The receiver app implements cyclic redundancy checks to detect corrupted packets and to drop them. Error correction algorithms, such as belief propagation and alternating direction method of multipliers[34], represent possible mechanisms that may further reduce the packet error rate in future work.

Mechanical properties, wireless power transfer, sensors and stimulators

The body of the device is mechanically flexible (Fig. 2a). The serpentine interconnects can stretch by as much as 40%, where the maximum strains reach 0.55% in the copper, as illustrated by the finite-element analysis (FEA, Supplementary Note 3) results in Fig. 2b (right) and Supplementary Fig. 5. The device consumes 2.8 mW of power with the μ-ILED probes off and 5.5 mW with the μ-ILED probes on and operating at a 50% duty cycle (Extended Data Fig. 1). The supercapacitors effectively mitigate brief surges of current from the power source during BLE transceiving events from -15 mA to -2 mA (Extended Data Fig. 1), thereby alleviating transient demands from wireless power transfer. The amount of wirelessly received power depends on the RF power supplied to the primary antenna, the location of the device in the cage, and the angular alignment between the primary and receiver antennae. Results in Fig. 2c obtained with a double-loop primary antenna located
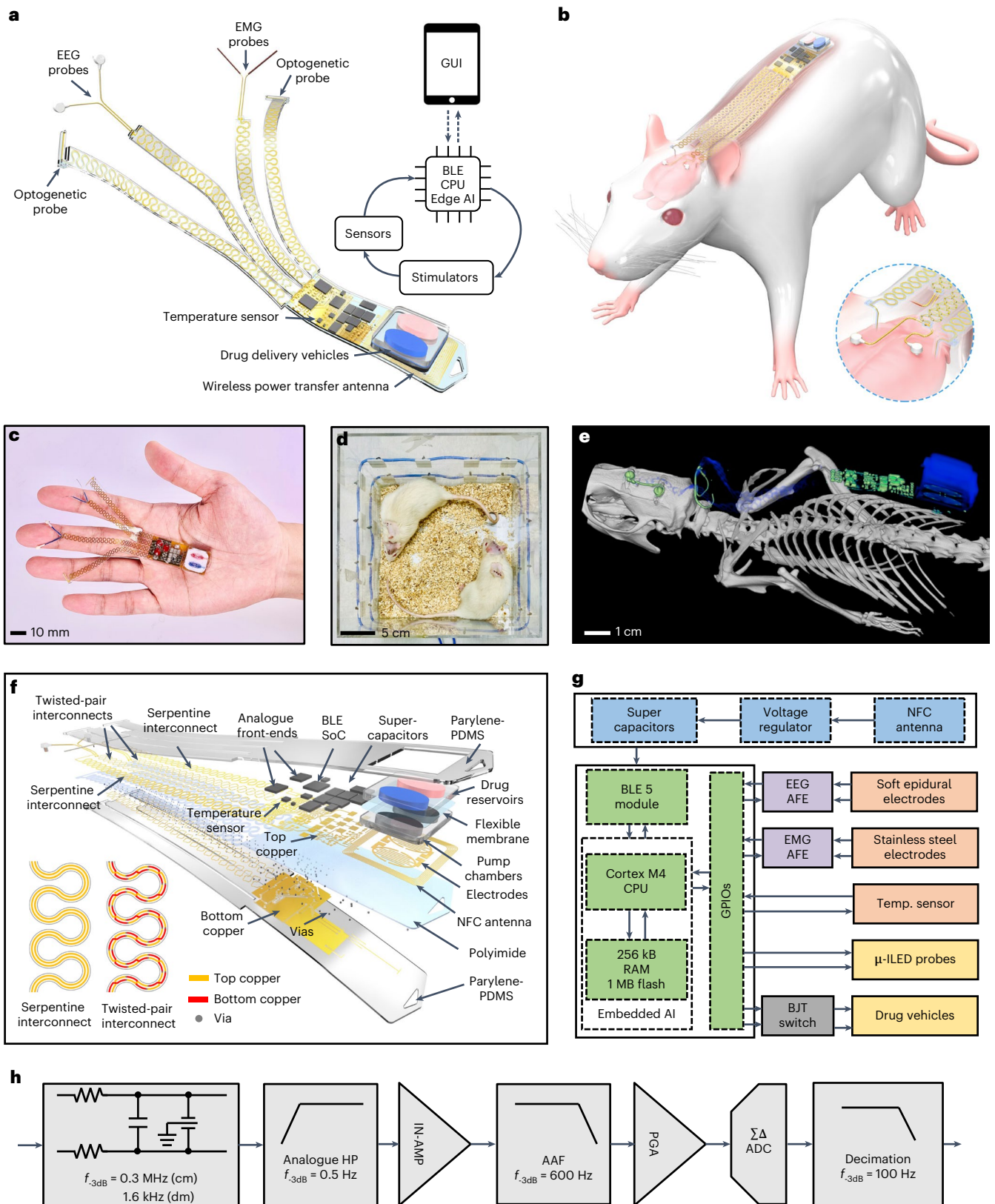
Fig. 1 | Device concept, implantation and architecture. a, Schematic illustration of the device and key functionalities. **b**, Schematic illustration of a device subdermally implanted in a rat and magnified view of the placement of sensors and stimulators. **c**, Photograph of an encapsulated device resting on the palm. **d**, Photograph of two implanted rats freely behaving and interacting in an NFC-powered setup. An NFC signal generator supplies power to the device via a double-loop primary antenna encircling the cage. **e**, Micro-CT image of an implanted device (side view). EEG and EMG electrodes insert into the skull and neck muscle, respectively. Optogenetic probes are not implanted in this example. **f**, Layered schematic illustration of the device. **g**, Electrical architecture of the device, including power management circuits, a BLE SoC with embedded AI, analogue front-ends and sensors (EEG, EMG, temperature) and stimulators (drug delivery vehicles, optogenetic probes). **h**, Signal conditioning flow for high-fidelity acquisition of biopotentials with low electromagnetic interference.

at heights of 6 cm and 11 cm indicate that the received power is strongest in the immediate vicinity of the antenna and weakest at the centre of the cage. At an RF input power of 4 W, the minimum power received by the device is 11 mW at the centre of the cage (height: 6 cm), multiples more than that required for steady operation (2.8 mW).

Results from simulations of an animal rearing up using an adult rat model placed at the corner and centre of the cage (Supplementary Note 4 and Extended Data Fig. 2a–c) show that the received power generally decreases with the rearing angle (Fig. 2d). While such motions of rats typically last 1–3 s, tests under extreme conditions where the rat holds a rearing angle indefinitely, as shown in Fig. 2e, provide insights into the resilience of the wireless power supply with onboard supercapacitor backup. With the μ-ILED probes off and a rearing angle as large as 70 degrees, the device can operate continuously without interruption. Operation is possible for 70 s and 50 s at rearing angles of 80 degrees at the corner and centre of the cage, respectively, until the supercapacitors discharge below the operating voltage of the BLE SoC (1.7 V). With the μ-ILED probes operating at a 50% duty cycle, the device can operate continuously with a rearing angle of up to 50 degrees; operation is possible for 37 s and 27 s at a rearing angle of 80 degrees at the corner and centre of the cage, respectively. Extended Data Fig. 2d–i show additional results when the input RF power is 2 W and 6 W. The collective results indicate reliable wireless power supply even during extreme animal motions. An additional concern is the effect of parasitic heating of the device in the animal determined by the balance between received power, consumed power and heat dissipation. Results from infrared imaging of implanted devices in anaesthetized animals (Supplementary Figs. 7 and 8) show that the peak increases in the skin temperature remain below ~1.2 °C at the receiver antenna under an input RF power of 4 W (default power for device operation unless otherwise specified), within the limit of a chronic temperature increase of 2 °C for implanted devices recommended by the American Association of Medical Instrumentation and supported by relevant in vivo thermal studies[35]. Open-field tests presented in a subsequent section suggest no observable behavioural change from the temperature increase. Reducing the Joule heating effect by optimizing the thickness and width of the copper traces of the receiver antenna and increasing thermal dissipation by optimizing the layout of the bottom copper layer represent possible strategies to further reduce the temperature at the receiver antenna. The device heating does not affect the temperature sensor (Supplementary Fig. 9), which is far from the receiver antenna in the device layout.

Implantation of standard stainless-steel EEG screws, for purposes of comparison, involves a two-step process that requires careful insertion of the screws into small pilot burr holes in the skull, followed by soldering leads to a headpiece or pin connection[36,37]. As mentioned previously, the system introduced here uses specially designed, miniaturized, soft EEG electrodes that bypass the need for bulky headpieces and connections (Fig. 2f,g). Each electrode (0.9 mm diameter) consists of a polyimide thin film with a bilayer of Cr (10 nm)/Au (100 nm) mounted on the surface of a cylindrical PDMS post (diameter × height: 1.2 mm × 1.75 mm). A chronoamperometry deposition process forms films of platinum black (PtBk) and polydopamine (pDA) in a layer-by-layer fashion on the bare gold surfaces[38]. The Methods and Supplementary Fig. 10a–c describe the fabrication process in detail. The large surface area of the PtBk-plated Au (Supplementary Fig. 10d) lowers the impedance from 400 kΩ to 5 kΩ at 1 Hz and from 40 kΩ to 1 kΩ at 1 kHz (Supplementary Fig. 10e). The pDA layers substantially enhance the mechanical integrity of the porous PtBk, as evidenced by invariant operation even after extended periods of sonication (Supplementary Fig. 10f). EEG recordings from a rat model allow comparisons of these electrodes to conventional screws (described in the Methods and illustrated in Supplementary Fig. 11). Acute testing during different physiological states in Extended Data Fig. 3 (awake, slow-wave sleep, fatal plus onset and euthanized) indicate that EEG signals recorded

using these soft electrode structures with PtBk/pDA are the same, to within uncertainties, as those collected using traditional stainless-steel screw electrodes. Continued testing for up to 2 weeks indicates the chronic stability of operation, as shown in Fig. 2h. The EMG electrodes use conventional stainless-steel wires connected to serpentine interconnects via short silicone-coated stainless-steel helical interconnects that provide freedom of placement in the neck muscles (Fig. 2i). Figure 2j highlights a comparison between temperature data collected from the on-device temperature sensor and that from a precision thermocouple placed at the same location in a water bath during a heating and cooling cycle (correlation: >0.999, Supplementary Note 5).

Each of the two optogenetic probes incorporates a μ-ILED (270 × 220 × 50 μm) at the tip end of a narrow filament of PI (350 μm × 75 μm × 6 mm) that supports copper electrical leads (thickness 18 μm), as shown in Fig. 2k. The system reported here uses blue (wavelength: 460 nm) μ-ILEDs for demonstration purposes (Supplementary Note 6 and Fig. 12). A tungsten needle (thickness 50 μm) on the back side of the PI filament provides mechanical reinforcement to facilitate implantation into the deep brain and to enhance thermal spreading to minimize increases in temperature associated with operation of the μ-ILEDs. A bilayer encapsulation of PDMS (thickness 30 μm) and parylene (thickness 30 μm) provides electrical insulation and a barrier to biofluid penetration. The system allows for wireless real-time programming of the duty cycle and frequency, over a range from 0% to 100% and 1 Hz to 100 Hz, respectively, thereby addressing nearly all requirements in optogenetics[39–41]. Extensive characterization and in vivo validation of optogenetic probes identical to those reported here demonstrate their biocompatibility and versatility for optogenetics studies[10]. Additional benchtop demonstrations of simultaneous bilateral optical stimulation and electrical recording in PBS that simulate electrical conduction in the body of a rat (described in Methods) exhibit no interference between the two modalities (Extended Data Fig. 4 and Supplementary Video 1). These results indicate potential for closed-loop optogenetic stimulation and neurorecording using methodologies established in this work for seizure mitigation.

The drug delivery component of the system consists of a pair of drug delivery vehicles, each made of interdigitated electrodes, an electrolyte chamber, a flexible membrane, a drug reservoir with a volume of 80 μl and microfluidic channels (Fig. 2l)[42]. The BLE SoC independently controls these vehicles through BJT switches (Supplementary Fig. 4). To deliver the drug, an electric current flows through the electrodes to initiate an electrochemical reaction known as electrolysis of water that generates hydrogen and oxygen. The gases accumulate in the electrolyte chamber and pressurize the bottom of the flexible membrane, which then deforms into a spherical cap and pumps the drug out through microfluidic channels (Fig. 2m). The rate of drug delivery is programmable by the rate of gas generation via tuning the voltage applied between the electrodes and the composition of the electrolyte (Supplementary Note 7 and Fig. 13). With a voltage of 2.0 V and 100 mM PBS as the electrolyte, the drug delivery vehicle delivers >99% of the drug within 120 s with a current consumption of ~5 mA (Fig. 2n and Extended Data Fig. 5), within the amount of power provided by an input RF power of 6 W (Extended Data Fig. 2).

In vivo validation of the neurorecording capabilities

The first set of tests involves measurements conducted simultaneously with those enabled by conventional tethered hardware (Neurosys), using EEG signals detected by a common set of electrodes in individual animals, as depicted in Fig. 3a and Supplementary Fig. 14. This protocol uses stainless-steel EEG screws inserted into the skull and mated to a 6-pin connector (P1 Technologies) surgically affixed to the head of the animal. A custom-fabricated Y connector bifurcates the signal from the EEG electrodes to provide both acquisition systems (tethered and wireless) with access to identical signals. Following at least 10 min of baseline recordings, experiments to evaluate low-frequency
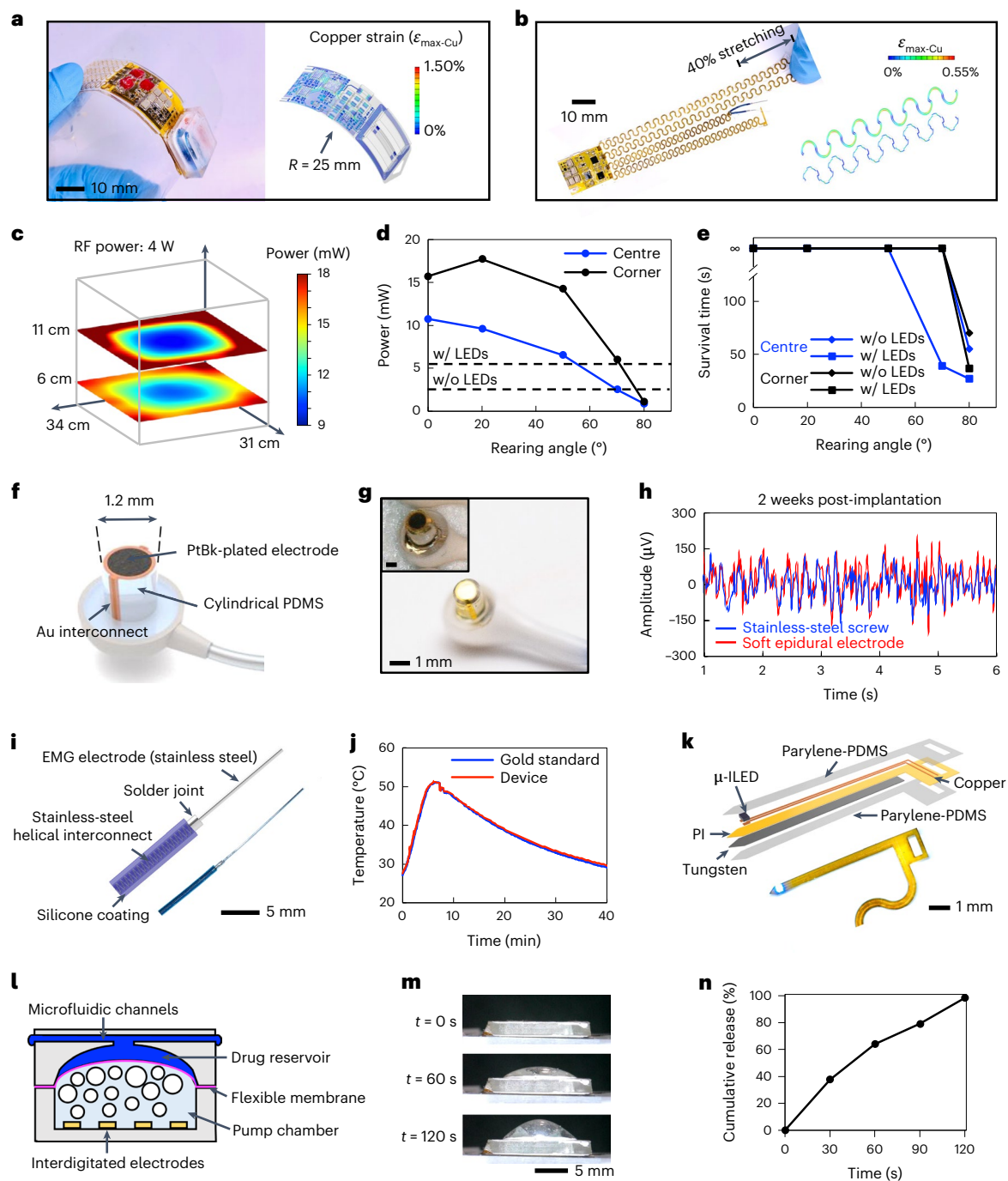
Fig. 2 | Characterization of the mechanical properties, wireless power transfer, and neurorecording and neuromodulation modalities.
a, Photograph of the device under bending and finite-element analysis of the bending characteristics. **b**, Photograph of stretching the serpentine interconnects and finite-element analysis of the stretching characteristics. **c**, Power received by the device at different positions of the testing cage at heights of 6 cm and 11 cm. **d**, Power received by the device at the centre and corner of the cage when the rat rears with different angles. **e**, Survival time (continuous recording time) of the device at the centre and corner of the cage when the rat holds rearing angles for an extended period with and without activating the bilateral μ-ILEDs. **f**, Schematic illustration of

the soft epidural gold electrode coated with platinum black (PtBk) for EEG recording. **g**, Photographs of the soft epidural electrode before and after (inset) electroplating of PtBk. **h**, Comparison of EEG signals measured by a soft epidural electrode and a conventional stainless-steel screw 2 weeks post-implantation. **i**, Schematic illustration (top left) and photograph (bottom right) of the EMG electrode. **j**, Comparison of the miniaturized temperature sensor of the device and a gold-standard temperature sensor in a heating-cooling cycle. **k**, Schematic illustration (top left) and photograph (bottom right) of the μ-ILED probe. **l**, Schematic illustration of the electrolysis pump-based drug delivery vehicle. **m**, The expansion of the flexible membrane with the generation of gas bubbles. **n**, Cumulative release of drug over time.

spikes involve administering the γ-aminobutyric acid type B (GABAB) agonist baclofen (10 mg kg^{-1}, intraperitoneal (i.p.); $n = 3$ rats). Baclofen hyper-synchronizes EEG activity to create high-amplitude

low-frequency spiking activity, as a means to track acute and dynamic changes in the recorded signal[43]. In a separate cohort of rats ($n = 3$ rats), the pilocarpine seizure model (400 mg kg^{-1}, i.p.) tests capabilities in

capturing EEG responses with higher frequency and amplitude. In all instances and animals, raw signals from each acquisition system overlap almost perfectly during baseline, baclofen- and pilocarpine-modulated periods (Fig. 3a and Extended Data Fig. 6a). The spectrograms in Fig. 3b and Extended Data Fig. 6b indicate indistinguishable power and frequency responses, as the EEG amplitude increases from ~100 μV to ~1,000 μV peak-to-peak during pilocarpine-induced seizures. Further, in all conditions, plots of the power as a function of frequency (Extended Data Fig. 6c,d) show near-perfect correlations (Pearson correlations ≥ 0.995).

EEG is a nonlinear and nonstationary signal comprising multiple oscillatory brain rhythms corresponding to different aspects of cognitive processes. Empirical mode decomposition (EMD) is an analysis technique for single-channel EEG that decomposes it into separate oscillations known as intrinsic mode functions (IMFs) that are thought to underlie different cognitive processes[44]. EMD analysis and corresponding instantaneous frequency characteristics by Hilbert-Huang transform during baseline (Supplementary Fig. 15), baclofen stimulation (Supplementary Fig. 16) and pilocarpine stimulation (Supplementary Fig. 17) show that EEG data collected by the tethered and wireless systems exhibit similar IMFs and instantaneous frequency characteristics, further confirming the similar signal quality of the two systems.

The second set of validation experiments involves implanting fully encapsulated devices in their final intended configurations (n = 3 rats), with no external connectors or tethers. Extended Data Fig. 7 highlights EEG measurements 3 d after surgery from an awake, freely behaving rat in different states from baseline, to pilocarpine drug onset and ultimately seizures. The EEG waveform shapes, frequency and power distributions are all within expectation based on previous experiments and experience.

Recording EEG responses to auditory stimuli, known as AEPs, in freely behaving rats (n = 3 rats) provides further validation of the EEG signal characteristics (Fig. 3c). Recording AEPs poses a challenge for any EEG recording system, as they are typically lower in amplitude than background EEG signals yet consist of reproducible waveforms with positive and negative peaks, latency, amplitude and behavioural correlation. The recording setup involves an acoustic sound attenuating chamber (Supplementary Fig. 18) that houses the wireless testing cage and a speaker that plays a programmed pure-tone auditory stimulus train (5/10 kHz, 75/85 dB, stimulus duration of 100 ms, inter-stimulus intervals pseudo-randomly varying between 5 and 10 s). Averaged responses from 10 trials produced AEPs with a positive peak at a latency of ~30 ms (P30), a negative peak at a latency of ~50 ms (N50) and another positive peak at a latency of ~120 ms (P120)[45]. The wireless system also captures the dependence of the amplitude of AEPs on the frequency and amplitude of the auditory stimulus, as reported previously[46].

Behavioural analysis and continuous recordings

The open-field test is a standard behavioural assay in neuroscience and pharmacology that assesses locomotor activity, anxiety-related and exploratory behaviour of rodents[47]. By testing animals' response to a new environment, this test quantifies the similarity of behaviour and underlying stress between different groups of animals through several behavioural parameters. Specifically, decreased locomotor activity (distance travelled and head speed), increased thigmotaxis (time spent in the outer zone (the outer 75% area of the cage)), increased freezing time, decreased unsupported rears (animal rearing without contacting the walls of the arena) and increased faecal boli count are indicative of increased stress[48–50]. The experiments use an overhead camera to record the movement of rats in the wireless testing cage (Fig. 4a). A deep learning model trained using the DeepLabCut package allows tracking of the head and tail to quantify animal motions[51] (Fig. 4b). Figure 4c,d show the head tracks of a naïve rat (control) and those of a rat 1 week following device implantation, respectively, during an 8-min period. Implanted rats (n = 6 rats) and naïve rats (n = 6 rats) exhibit almost identical travel

distances (P = 0.9513; Fig. 4e) and head speeds (P = 0.9286; Fig. 4f). The time spent in the outer and inner zones (P = 0.5833 and P = 0.7189 for outer and inner, respectively; Fig. 4g), the unsupported rear count (P = 0.8036; Fig. 4h), the freezing time (P = 0.9291; Supplementary Fig. 19a) and the faecal boli count (P = 0.8174; Supplementary Fig. 19b) are also similar between implanted and naïve rats. These results collectively indicate that implanted rats behave similarly to naïve rats. Changes in body weight (n = 3 rats) indicate normal growth patterns in weight for more than 60 d post-implantation (Supplementary Fig. 20).

High-quality continuous neurorecordings from freely moving, minimally perturbed animals create many opportunities for neuroscience research, including studies of sleep–wake regulation. Figure 4i presents the results of synchronized recordings of EEG and EMG data for a 1-h period from a rat at 1 week post-implantation as a demonstration of continuous neurorecording capabilities in freely moving animals. The results capture 3 stages of sleep status with the following features:[52,53] wakefulness characterized by low-amplitude EEG, medium power in the delta band (0.5–4 Hz) and theta band (6–9 Hz), and high EMG activity (Extended Data Fig. 8a); non-rapid eye movement (NREM) sleep characterized by high-amplitude EEG, high power in the delta band, low power in the theta band and low EMG activity (Extended Data Fig. 8b); rapid eye movement (REM) sleep characterized by low-amplitude EEG signal, low power in the delta band, high power in the theta band and low EMG activity (Extended Data Fig. 8c). EMD analysis of EEG further reveals different oscillatory processes involved in different sleep stages (Extended Data Fig. 9). On the basis of these criteria, expert scoring on non-overlapping 30-s epochs of the EEG-EMG data reveals the dynamics of sleep stage transition (Fig. 4i). Chronic tests illustrate capabilities for high-quality EEG-EMG recordings for at least 6 weeks post-implantation (Fig. 4j), with well captured dynamics of sleep stages throughout. Observations indicate a device survival rate of 83.3% for 6 weeks post-implantation in a chronic study that lasted 10 weeks with a group of 6 animals (Supplementary Fig. 21). In a separate group of 2 animals, devices explanted at 6 weeks show good integrity of the encapsulation layers and full functionality (Supplementary Fig. 22). Subsequent failure of devices after 6 weeks, examined through a workflow shown in Supplementary Fig. 23, results from failure of the BLE module due to fracture of solder joints under mechanical stress—one of the most common causes of failure of ball grid array chips. Further benchtop bending cyclic tests suggest improved mechanical reliability through the addition of an FR-4 stiffener under the BLE chip on the bottom side of the fPCB to enhance the bending stiffness of this region (Supplementary Fig. 24).

Sleep–wake-regulation studies

Figure 5a shows overnight (6.5 h light and 12 h dark) recordings from a rat at 1 week post-implantation in a temperature- and humidity-controlled room with a 12 h:12 h light-dark cycle (light: 6:00–18:00). The data during light and dark periods show normal sleep–wake patterns that differ across the light periods. During the light period (Fig. 5a), the EEG signal primarily exhibits high-amplitude and low-frequency content, while the EMG signal shows low activity, that is, features of NREM sleep, with intermittent REM sleep and wakefulness epochs. In contrast, during the 12 h dark period (Fig. 5a), the EEG signal exhibits low-amplitude and medium power in the delta and theta bands, while the EMG signal indicates high activity, consistent with the dominance of wakefulness and mobility. The body temperature (subcutaneous) of the rat correlates well with its activity level, with a near constant temperature of 37.0 °C during the light periods and nocturnal temperatures up to 38 °C during periods of high activity, all consistent with known patterns of temperature regulation in rats[54]. The results in Fig. 5b show that the percentages of wakefulness, NREM sleep and REM sleep during the light period are 22%, 67% and 11%, respectively, while those during the dark period are 76%, 21% and 3%, respectively. When scaled to a total time of 24 h, wakefulness is 49% of the total time and sleep is 51%. Figure 5c
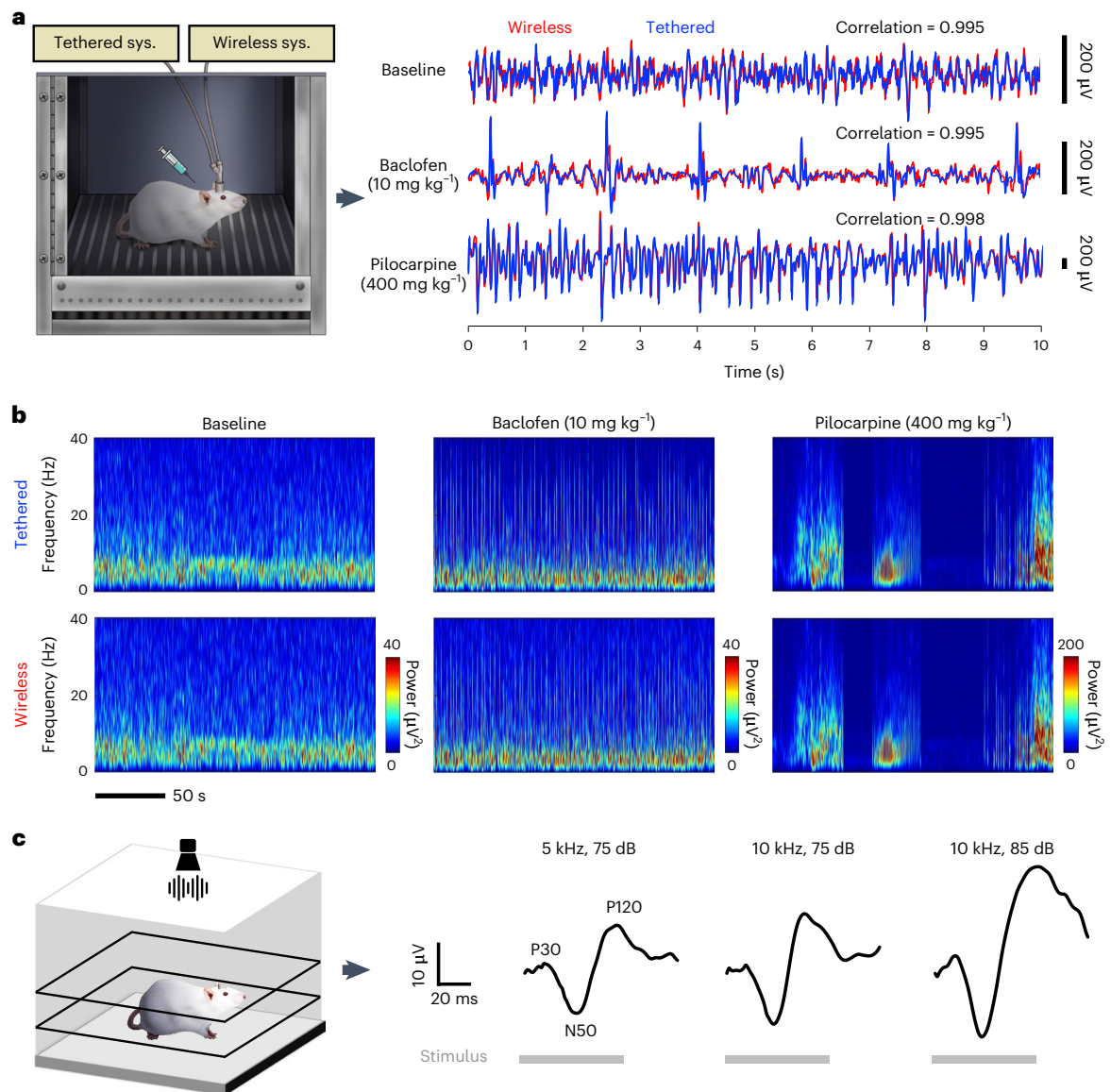
Fig. 3 | Validation of the wireless neurorecording functionality by pharmaceutical and auditory stimulation and comparison to a conventional tethered system. a, Schematic illustration of the A/B test setup in which the wireless and tethered systems are directly compared through a signal splitter and comparison of the time-domain EEG data under different drug stimulations. **b,** Spectrograms showing near identical frequency- and time-domain features of the wireless and tethered systems under different conditions. **c,** Under puretone sound stimulations, EEG data measured by the wireless device show typical auditory-evoked potentials.

presents the mean epoch durations of the 3 stages, indicating typical REM sleep durations of ~2 min, longer NREM sleep epochs during the light period and longer wakefulness epochs during the dark period. All values are in good accordance with those of previous studies of sleep–wake patterns of normal rats[55,56].

Autonomous closed-loop neurorecording and neuromodulation

Neurosignal pattern recognition and quantification algorithms based on AI approaches can be deployed directly on the BLE SoC (64 MHz CPU, 256 kB RAM, 1 MB flash) to enable closed-loop control of neuromodulation. A two-step process (Fig. 6a) involves training a deep learning model on a GPU-accelerated workstation to generate a compressed executable, followed by uploading it to the BLE SoC to form an optimized data pipeline that performs data pre-processing, deep learning inference and closed-loop control with limited computing resources. The demonstration illustrated here adopts a CNN because it achieves a balanced performance for seizure detection with good accuracy and moderate computation complexity compared with artificial neural network (ANN) and long short-term memory (LSTM) models[21]. The training exploits an existing labelled dataset consisting of 30,000 3 s samples of normal EEG and 30,000 3 s samples of seizure EEG in rats and mice extracted from telemetry recordings provided by Open Source Instruments. Short time Fourier transform (STFT) of time-series data into spectrograms, each with a shape of 35 × 31 and normalized by the total power at each time bin to eliminate biases from signal amplitude, forms the features for training. The CNN model involves only 12,002 parameters and 300,000 multiply-accumulate (MAC) operations, sequentially consisting of a two-dimensional (2D) convolution layer with a kernel shape of 7 × 7 × 8 and rectified linear unit (ReLU) activation, a fully connected layer with an output of 2 neurons and ReLU activation, and a Softmax layer as the final output layer. The design and optimization considerations for the CNN model are described in detail in Methods. The training process uses an ADAM optimizer and
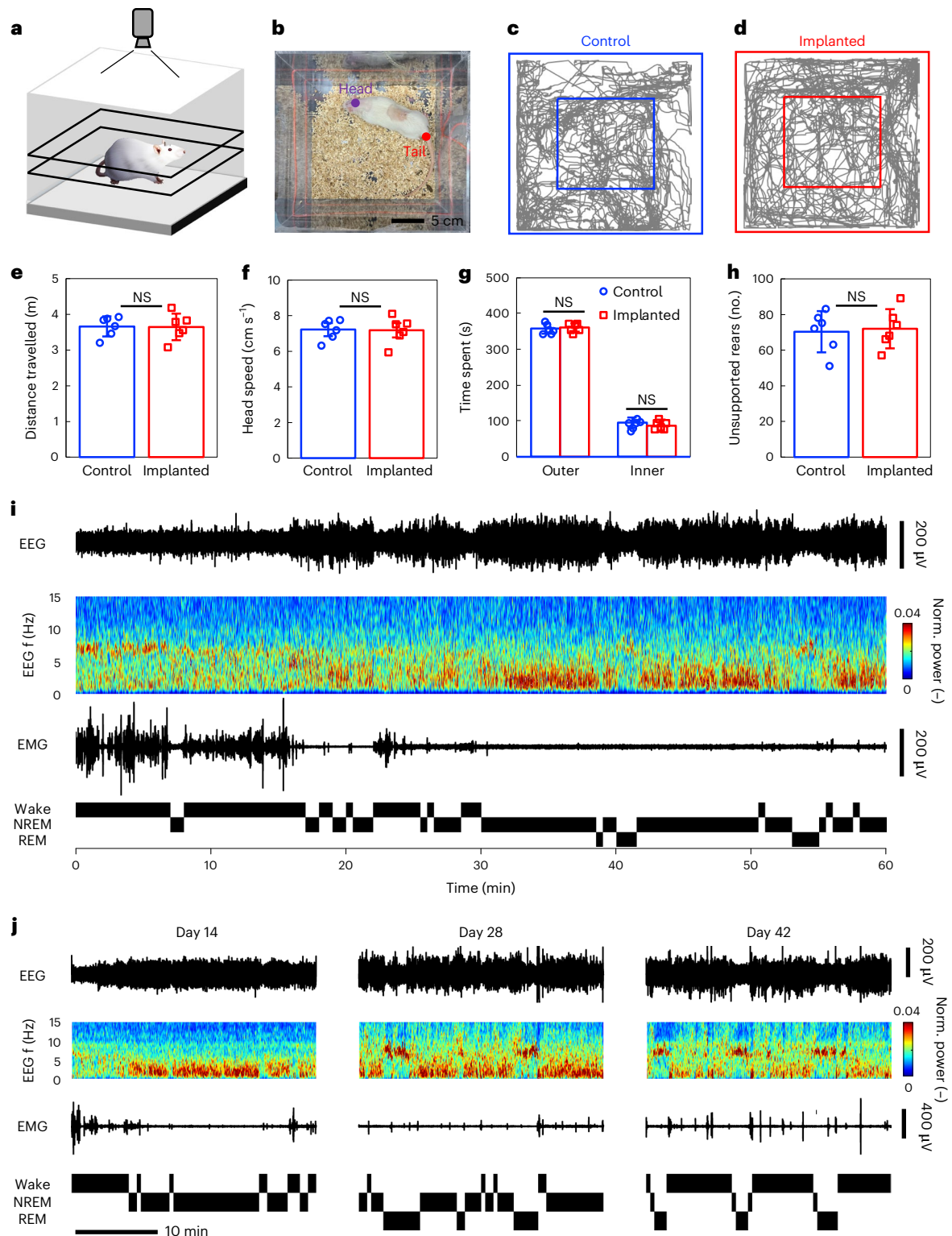
Fig. 4 | Open-field tests of rat locomotor behaviours, neurorecording in a freely behaving rat and chronic stability of neurorecording of a fully implanted device. a, Schematic illustration of the testing setup. **b**, Video snapshot of motion tracking by deep learning. **c**,**d**, Head traces of a control rat without the implanted device (**c**) and an implanted rat (**d**) for a duration of 8 min. **e**–**h**, Statistical comparisons of the behaviours of control and implanted rats using two-tailed Student's *t*-tests: distance travelled (**e**), average head speed (**f**), time spent in the outer and inner zones of the cage (**g**) and unsupported rear count (NS, not significant; all data are represented as mean ± s.e.m.; $n = 6$ rats for control rats and $n = 6$ rats for implanted rats; $P < 0.05$ is considered statistically significant) (**h**). **i**, Representative synchronized EEG and EMG recording in a freely behaving rat at 7 d post-implantation during REM, NREM and wakefulness. **j**, Chronic stability of EEG and EMG recording for up to 42 d during REM, NREM and wakefulness.
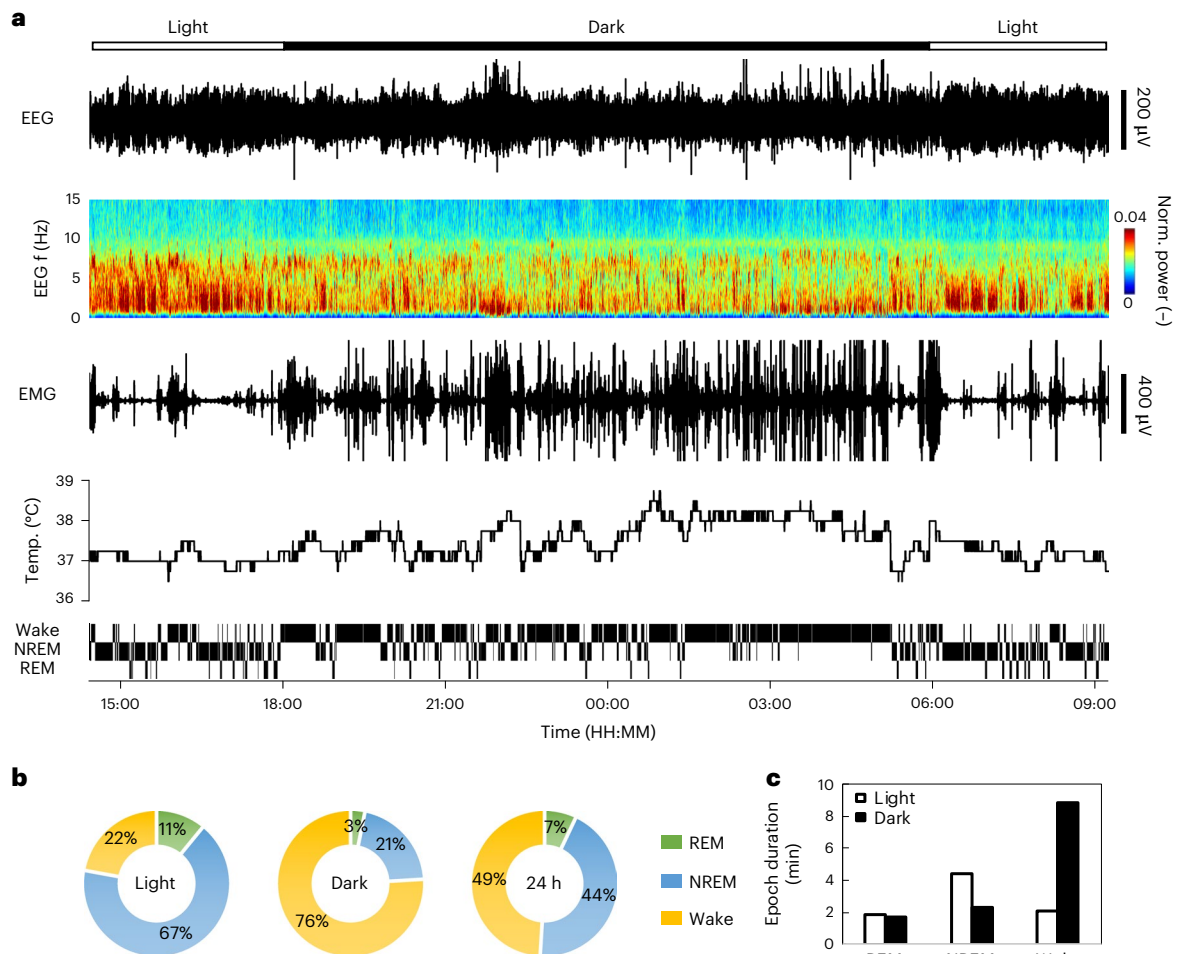
Fig. 5 | Sleep–wake regulation studies in a freely behaving rat. a, Synchronized overnight recording of EEG, EMG and temperature, and resulting sleep staging analysis. **b**, Percentage of time in REM, NREM and wakefulness during light and dark periods. **c**, Mean epoch durations of REM, NREM and wakefulness during light and dark periods.

a random dataset split of 60%: 20%: 20% for training, validation and testing. The model at the checkpoint with the minimum validation loss serves as the final model, showing a validation accuracy of 0.97 for distinguishing seizure and non-seizure epochs (Extended Data Fig. 10). Conversion of the CNN model to a tiny model (14 kB) involves post-training quantization of the model parameters from 32-bit floating points to 8-bit integers. The quantized model shows minimal loss of accuracy, with an area under the curve of 0.97 (Fig. 6b) and overall prediction accuracy of 0.92 (Fig. 6c). The on-device inference uses the TensorFlow Lite for Microcontrollers framework described in detail in Methods and Supplementary Fig. 25 (ref. 25). The data pipeline on the BLE SoC loads every 1.5 s the latest 3 s EEG (1.5 s overlap) signal for transformation into a spectrogram using a C++ STFT library. The interpreter then performs inference on the spectrogram in an allocated memory arena utilizing the tiny model and a neural network operations resolver based on ARM's high-efficiency CMISS-NN neural network operation library. The output of the interpreter is a seizure score in the scale of 0–256, based on which a responder function executes the control policy shown in Fig. 6d. The responder determines the onset of seizures when the average seizure score of the latest 30 s (involving 20 consecutive inferences) is above 128 and then issues the release of the anti-seizure drug (midazolam, 1 mg kg^{-1}) if it is the first dose or if 10 min has passed since the release of the previous dose. The responder also supports human-override privileges for ethical considerations in case drug release does not trigger correctly. The programme fits within the

constrained memory and storage of the SoC with an execution time of 58.7 ms (Supplementary Fig. 25), from EEG data loading, spectrogram generation, to CNN inference and command issuance. The device consumes an average power of 2.6 mW in autonomous mode, with a brief peak power of 6.8 mW for 54.2 ms during AI inference (Supplementary Fig. 26). The short execution time and low power consumption ensure stable operation of the device and instant seizure detection.

In vivo validation of this autonomous seizure management system involves rats (n = 5 rats) with pilocarpine-induced seizures (Fig. 6e–g). In a typical control experiment that uses a device loaded with 2 doses of saline (80 µl each, Fig. 6e), the rat develops epileptic seizures following the injection of pilocarpine (400 mg kg^{-1}). Triggering the release of the first dose of saline at the onset of seizures does not mitigate seizures and after 10 min (seizure score at ~256), the device triggers the release of the second dose of saline. As anticipated, seizures persist 10 min after this second dose of saline, which leads to euthanization of the animal according to the Institutional Animal Care and Use Committee (IACUC) protocol. In an experimental group that involves a device loaded with 2 doses of midazolam (Fig. 6f), triggering the release of the first dose of drug release at the onset of epileptic seizures reduces seizures within a few minutes. Recurring seizures identified by the on-device AI then trigger the release of a second dose of midazolam, which suppresses seizures for the remaining period of the experiment (90 min) outside of a brief burst of seizures shortly after the release of the drug. In another animal (Fig. 6g), the subject appears to exhibit an extended pre-onset
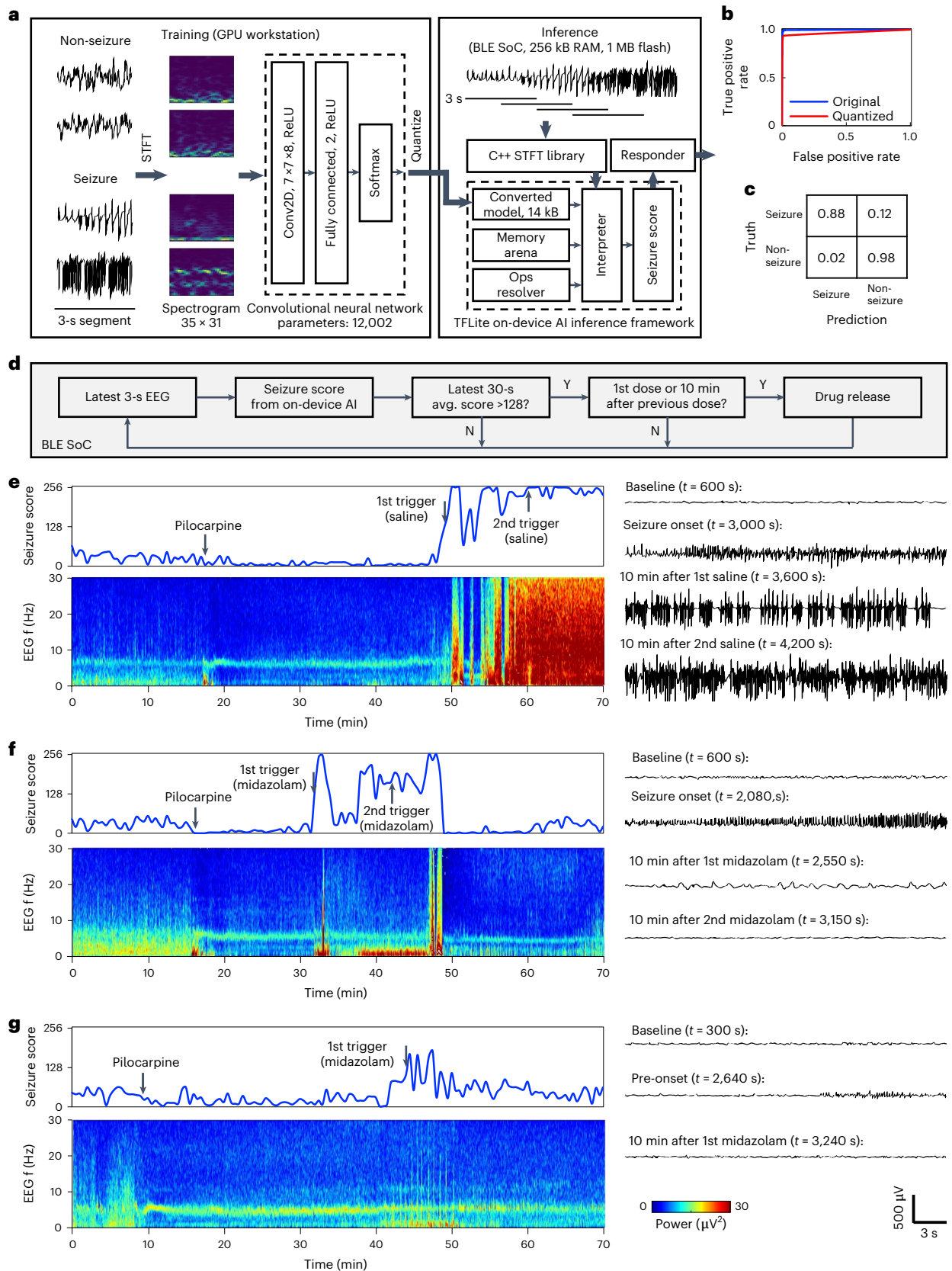
Fig. 6 | Autonomous seizure management. a, Training of a seizure detection neural network model and implementation of the quantized model onto the BLE SoC for on-device AI. **b**, Receiver operating characteristic curves of the original and quantized models. **c**, Confusion matrix of the on-device AI model. **d**, On-device algorithm for real-time closed-loop management of seizure. **e**, Saline-release control study in a rat model. Seizure score, spectrogram and magnified time-series EEG demonstrate autonomous release of 2 doses of saline and persistence of seizures. **f**, In a second rat model, seizures were mitigated by autonomous release of 2 doses of midazolam upon detection of seizures. **g**, In a third rat model, an extended pre-onset phase of seizure was detected and mitigated by autonomous release of 1 dose of midazolam.

seizure stage following the pilocarpine administration. Initial seizure activity detected by the on-device AI triggers the release of the first dose of midazolam. This effectively prevents the onset of epileptic seizures for the remainder of the experiment, with the second dose being unused and therefore available for a potential seizure recurrence at a later time point.

Discussion

We have described a wireless, battery-free and fully implantable system in a miniature and flexible form factor compatible with small animal models, with diverse capabilities in neurorecording and neuromodulation, including autonomous closed-loop operation enabled by on-device AI. The system supports excellent performance and chronic stability for at least 6 weeks, in a manner that minimally perturbs the naturalistic behaviours and responses of freely moving and interacting animals. The back-mounted electronics hub with serpentine interconnects to sensors and stimulators is easily adaptable to address a range of application possibilities beyond those presented here. For example, probes interfaced with the cardiac, gastrointestinal and peripheral nervous systems can be used in studies of their respective functions. Extended versions may also integrate multiple biophysical (such as blood pressure, oxygen saturation and respiration) and/or biochemical sensors (for proteins, nucleic acids or metabolites, for example) with various types of stimulator (such as electrical, optical or pharmacological), as shown in related technologies[57–61]. The development of application-specific integrated circuits and the use of doubled-sided fPCB layouts may result in devices with substantially reduced size and weight for future use in mouse models.

Some of the most compelling and immediate opportunities for use in neuroscience research are in unconstrained behavioural studies, especially those involving social interactions and those prone to stress-induced artefacts. Investigations of sleep–wake regulation processes through synchronized EEG, EMG and temperature create possibilities for studying regulatory mechanisms of circadian rhythms and sleep–wake homoeostasis. Programmable drug delivery can be used to examine pharmacologically induced effects on these processes. Physiological measurements of mechanisms associated with formation of dominance hierarchies, development of bonding and mating behaviours and others are also promising directions. Neural networks, such as those implemented in the devices reported here, offer utility in the generalizable recognition of these sophisticated and subtle patterns of activity. Extensions of the basic ideas introduced in this work, such as the thin flexible geometries and the wirelessly powered capabilities in neurorecording/neuromodulation and on-device computation, may also lead to systems designed for therapeutic and/or diagnostic use in humans[4,62].

Methods

Electrical components

Small-footprint, off-the-shelf components served as the basis of the systems described here. A receiver coil on the fPCB paired with two tuning capacitors (1–100 pF) yielded a resonant peak at 13.56 MHz for wireless power transfer. High-speed Schottky diodes in a full-wave bridge rectifier followed by a first-order resistor-capacitor filter converted the inductively coupled AC voltage to a DC voltage. A low-dropout linear voltage regulator (ADP7112, Analog Devices) in 6-pin wafer-level chip-scale packaging (WLCSP) (1.2 mm × 1 mm) converted the DC voltage to a constant voltage supply (2.7 V) to power the system. An array of 6 supercapacitors (CPX3225A752D, Seiko Instruments) connected to the output of the voltage regulator provided a temporary power source in the event of compromised wireless power transfer. A BLE SoC (nRF52840-CKAA, Nordic Semiconductor) in WLCSP packaging (3.5 mm × 3.6 mm) served as the CPU, Bluetooth communication module and deep learning inference hardware. A second low-dropout voltage regulator (LP5907UVX, Texas Instruments) in 4-pin WLCSP

packaging (0.645 mm × 0.645 mm) connected to the output of the first voltage regulator provided a constant voltage supply of 1.8 V to the biopotential AFEs. Two ultra-low-power (180 μW), high common-mode rejection (>100 dB) biopotential AFEs (MAX30003, Maxim Integrated) in WLCSP packaging (2.74 mm × 2.9 mm) amplified, filtered and digitized the EEG and EMG signals and transmitted the digital data to the BLE SoC via the SPI interface. An ultra-low-power (25 μW) temperature sensor (MAX31875, Maxim Integrated) in WLCSP packaging (0.84 mm × 0.84 mm) measured the body temperature and transmitted digitalized data to the BLE SoC via the I2C interface. Two GPIOs of the BLE SoC with a current-limiting resistor in series powered the 2 μ-ILED probes, respectively. BJT switches (BC847 and BC857, Infineon Technologies) controlled by 2 GPIOs of the BLE SoC with a current-limiting resistor in series controlled the triggering of the two drug delivery devices, respectively. The BLE SoC used a miniaturized (3.2 mm × 1.6 mm) ceramic 2.45 GHz antenna (2450AT18A100, Johanson Technology) for data transmission. Other passive components with 0201 (imperial) packaging minimized the overall size of the system. Supplementary Table 3 lists detailed information on key components.

Fabrication of the soft epidural EEG electrodes

Electrode fabrication. The fabrication began with a glass substrate (75 mm × 50 mm) cleaned with acetone, isopropyl alcohol and deionized water and then exposed to ultraviolet-induced ozone (UVO) for 1 min. Spin-coating (2,000 r.p.m. for 30 s) and baking on a hot plate at 180 °C for 1 min formed a sacrificial layer of poly(methyl methacrylate) (PMMA, 950 PMMA A5, MicroChem). Spin-coating a solution of poly(pyromellitic dianhydride-co-4,4'-oxydianiline) amic acid (PI 2545, HD Microsystems) at 2,000 r.p.m. for 40 s, followed by pre-baking on a hot plate at 150 °C for 5 min and then fully curing in a vacuum oven at 250 °C for 75 min defined a layer of PI on top of the PMMA. Electron beam evaporation (AJA International) yielded a bilayer of Cr (10 nm)/Au (100 nm). Photolithography (photoresist AZ 1805; spin-casting at 3,000 r.p.m. for 30 s, baking on a hot plate at 110 °C for 1 min, exposing to UV light at a dose of 50 mJ cm^{-2}, developing for ~60 s with developer AZ 400K/deionized water solution in a 1:4 volume ratio) and etching with gold (TFA, Transene) and chromium etchants (CEP-200, HTA Enterprises) patterned the metal into the required geometries. Removing the photoresist with acetone and isopropyl alcohol, and spin-coating a layer of PI (1,000 r.p.m. for 40 s; baking and curing according to steps described above) completed the fabrication of encapsulated conductive traces. Depositing a layer of Cu with a thickness of 50 nm by electron beam evaporation, followed by photolithography and wet etching using procedures mentioned above defined a hard mask. Reactive ion etching (March RIE, 35 sccm O2, 210 mTorr, 200 W, 40 min) removed the PI on each gold EEG electrode (0.9 mm diameter) and connecting gold pad (1.2 mm diameter). Immersion in Cu etchant removed the Cu layer and washing in water completed the process.

Electrode assembly. Fabrication of the cylindrical pieces of PDMS (diameter × height: 1.2 mm × 1.75 mm) involved pouring a precursor to PDMS (Dow Corning Sylgard 184) into a Teflon tube (PTFE-28-25, SAI) with an inner diameter of 1.2 mm (Supplementary Fig. 9c), followed by curing in an oven at 100 °C and removing the tube. For the donut-shaped PDMS (inner diameter × outer diameter × height: 1.2 mm × 2.0 mm × 0.5 mm), a silicon wafer (Supplementary Fig. 9b) patterned by photolithography and deep reactive ion etching (DRIE, STS LpX Pegasus) served as a mould. Spin-casting of PDMS precursor material onto this mould (1,000 r.p.m. for 30 s), followed by curing in an oven at 100 °C and demoulding the PDMS completed the fabrication. The inner and outer parts of the PDMS were removed using mechanical punches with diameters of 1.2 mm and 2.0 mm, respectively, to form the donut-shaped structure. To fabricate an electrical connection to a flexible 1-cm-long helical wire (Open Source Instruments), a small droplet of solder was placed on a connecting gold pad (1.2 mm diameter) with

soldering flux applied with a pen, using a soldering iron at 325 °C. The gold EEG electrode was placed on top of the cylindrical PDMS, and the assembly was then passed through the inner hole of the donut-shaped PDMS by gently pressing the bottom of the cylindrical PDMS. The connecting gold pad with the solder droplet was secured by applying a small amount of PDMS precursor, followed by curing using a heat gun at 130 °C for 180 s. The fine wire was electrically connected by temporarily melting the solder droplet using a soldering iron at 325 °C. A layer of epoxy (Loctite Epoxy Marine, Henkel) encapsulated the system.

Electrochemical deposition of PtBk/pDA and measurement of electrolyte-electrode impedance. Deposition of PtBk and pDA occurred in a layer-by-layer fashion by chronoamperometry (PGSTAT128N, Metrohm Autolab) with a three-electrode system (Pt wire as the counter electrode and Ag/AgCl electrode as the reference electrode). Immersion of the assembled EEG electrode in a mixture of 3 wt% chloroplatinic acid (PtCl6H2, Sigma-Aldrich) and 0.1% lead acetate (Pb(C$_2$H$_3$O$_2$)$_2$, Sigma-Aldrich) enabled deposition of PtBk. A 2 mg ml^{-1} solution of dopamine hydrochloride (Sigma-Aldrich) in PBS (10 mM, pH 6.0) served as the basis for deposition of pDA. The total electrochemical deposition time for PtBk and pDA was 40 s and 1,500 s, respectively. A Pt wire and an Ag/AgCl electrode immersed into a 1x PBS solution (pH 7.4) and connected to an electrochemical impedance spectrometer setup (PGSTAT128N, Metrohm Autolab) allowed measurement of the electrolyte-electrode impedance at a frequency range of 1 Hz to 10 kHz for the EEG electrodes.

Connecting to the twisted-pair interconnect. Connecting a pair of PtBk-plated gold electrodes to the two pads of a twisted-pair interconnect via the helical wires by soldering concluded the fabrication of the EEG sensors.

Fabrication of EMG electrodes
The fabrication of the EMG electrodes involved insertion of a pair of 1-cm-long stainless-steel wires (0.008 inch diameter) into a pair of 1-cm-long helical wires (Open Source Instruments) by 1–2 mm and soldering of the joints with the aid of stainless-steel flux, followed by soldering the helical wires to the two pads of a twisted-pair interconnect.

Fabrication of the drug delivery vehicles
Fabrication of the microfluidic channels. The fabrication process started with formation of a mould in the geometry of the microfluidic channels by 3D printing (Form 3, Formlabs), followed by casting of PDMS (elastomer/curing agent ratio, 10:1; Sylgard 184, Dow Corning) and curing in an oven at 70 °C for 45 min.

Preparation of the flexible membrane. The fabrication started with dissolution of 30 wt% polystyrene-b-polyisoprene-b-polystyrene (SIS, Sigma-Aldrich) in toluene with sonication, followed by casting the SIS solution onto a silicon wafer pre-treated with mould release spray (Ease Release 200, Mann Release Technologies) and annealing at 60 °C for ~3 h.

Assembly of the drug delivery vehicles. Fabrication of the pump chambers and drug reservoirs (with outlet ports) involved 3D printing (Form 3, Formlabs). The assembly process involved aligning and bonding the pump chambers to interdigitated electrodes on an fPCB, followed by bonding the SIS flexible membrane between the pump chambers and drug reservoirs. The bonding process involved a commercially available sealant (3M marine adhesive sealant fast cure 5200) to prevent leakage and evaporation of the electrolyte. A PDMS (elastomer/curing agent ratio, 10:1; Sylgard 184, Dow Corning) encapsulation structure formed by a 3D-printed mould served to contain the assembled devices. Soft PDMS microfluidic channels were aligned to the outlet ports of the reservoirs and bonded to the top PDMS capping layer of the reservoirs by corona treatment. Sealing of the filling ports for the electrolyte and drug utilized a silicone adhesive (Kwik-Sil, World Precision Instruments).

Fabrication of the μ-ILED probes
Hot-air soldering using low-temperature solder (Indium) bonded μ-ILEDs (TR2227, CREE) to the respective pads. Bonding of tungsten stiffeners (50 μm, Sigma-Aldrich) patterned by laser ablation onto the back sides of the probes with a thin layer of epoxy (Devcon 5-min, ITW Performance Polymers) enhanced the mechanical rigidity to allow for controlled implantation into the deep brain.

Assembly and encapsulation of the device
Following hot-air soldering of electrical components to the fPCB, application of an epoxy adhesive (Loctite 3621, Henke) to the BLE SoC and MAX30003 AFEs and curing at 95 °C for 25 min provided mechanical protection for the chips. After adhering tungsten stiffeners to the μ-ILED probes, chemical vapour deposition formed conformal coatings of parylene-C (30 μm) to encapsulate the device. Exposing the soldering pads for the interdigitated electrodes by scraping with a razor blade and soldering the assembled drug delivery vehicles to these pads allowed for the assembly of the drug delivery vehicles onto the main device. Spin coating of PDMS (10:1 mixed) at 1,000 r.p.m. for 30 s formed an uncured layer of PDMS (100 μm thick) on a plastic substrate. Gently pressing the device into the uncured PDMS followed by curing at 75 °C for 20 min formed the PDMS encapsulation layer. Subsequent drop casting of uncured PDMS onto electrical components followed by curing at 75 °C for 20 min ensured full coverage of the components. Removing the PDMS coating layer from the optogenetic probe tips and subsequent dip coating in PDMS formed a thin layer of PDMS encapsulation (30 μm) suitable for deep brain implantation. Exposing the metal pads on the twisted-pair interconnects with a razor blade followed by soldering the helical wires of the EEG and EMG electrodes to the metal pads with a soldering iron completed the assembly of the electrodes.

Simultaneous optical stimulation and electrical recording
The device was submerged in PBS to simulate the electrical conduction in the body of a rat. The EEG electrodes and optogenetic probes were arranged in a similar configuration to that in animal studies. Simulated electrical signal was fed through PBS by a function generator that performed a cyclic frequency sweep up from 0.5 Hz to 100 Hz and then down from 100 Hz to 0.5 Hz using a constant amplitude. The device simultaneously performed bilateral optical stimulation at 5 Hz with a 50% duty cycle and electrical recording using the EEG channel. The amplitude of the input signal received by the device was ~100 μV at 50 Hz. Because of the higher impedance at the interface between the input electrodes of the function generator and PBS at lower frequencies, stronger attenuation of the input signal was observed at lower frequencies, with an amplitude of ~10 μV being received by the device at 0.5 Hz.

Animals
All experiments used adult Sprague Dawley rats (250–350 g at start of experiments) from Charles River Laboratories, maintained on a 12 h light/dark cycle and fed ad libitum. Rats were group housed (2–4 per cage) before surgery, after which each was individually housed in a climate-controlled vivarium. All experimental procedures were conducted in accordance with the National Institutes of Health standards and were approved by the IACUC at Northwestern University or the Medical University of South Carolina.

Surgical procedures
All procedures complied with Animal Welfare and IACUC policies under approved protocols using aseptic conditions. Animals were anaesthetized in an induction chamber (4–5% isoflurane). Once anaesthetized, the animals' head and back fur was shaved before placing them in a

stereotaxic frame (Kopf) with regulated heating pad. The animals were maintained at a surgical plane of anaesthesia using 2–3% isoflurane for the duration of surgery. Meloxicam (2 mg kg^{-1}, subcutaneous injection) and bupivacaine (2 mg kg^{-1}, intradermal injection) worked as preoperative analgesic. After the rat reached a stable plane of anaesthesia, a midline incision down the centre of the scalp exposed the skull, followed by a second ~10 mm incision midway down and across the back. Blunt forceps and scissors separated the subcutaneous fascia between the scalp and back incisions. The device was manually inserted into the posterior portion of the scalp incision and pulled posteriorly until it rested above the spine in a position where the midpoint of the device was located at the back suture line. Serpentine interconnects travelled subcutaneously across the neck region to connect the device body with the electrodes. Four burr holes were drilled in the skull with a variable-speed surgical drill to form implantation sites for the two µ-ILED probes and two EEG electrodes. The use of a stereotaxic holder (PH-300, ASI Scientific) facilitated implantation of the bilateral optogenetic probes. Probes were affixed to the skull with a cyanoacrylate adhesive to prevent probe movement. Implantation of EEG electrodes involved the placement of each electrode in a burr hole and with light downward pressure using a blunt 18 g needle in a stereotaxic holder. Application of cyanoacrylate around the perimeter of the sensor provided fixation to the skull. Stainless-steel EMG electrodes were inserted into the nuchal (neck) muscles with the aid of a 21 g needle. Lastly, sutures closed both incisions and the animals were allowed to recover for several hours before being transferred to the cage area facility for post-surgical monitoring. Buprenorphine SR (0.3 mg kg^{-1}, subcutaneous injection) was given postoperatively for long-term pain management. Device testing occurred after a minimum of 3 d of surgical recovery.

Microscale CT imaging
CT imaging with a preclinical microPET/CT imaging system (Mediso nanoScan scanner) used 'medium' magnification, 33 µm focal spot, 1 × 1 binning, 720 projection views over a full circle and a 300 ms exposure time. Reconstruction of projection data used a voxel size of 68 µm with filtered (Butterworth filter) back-projection software from Mediso Nucline (v2.01). Throughout the imaging process, a digital system developed by Mediso monitored respiratory signals.

Validation of soft epidural electrodes
These studies utilized three 250–350 g Sprague Dawley rats from Charles River Laboratories. Three burr holes were drilled into the skull to accommodate one common and two signal channel electrodes. A stainless-steel EEG screw was inserted into one hole and served as channel 1. Two soft epidural electrodes were inserted into the remaining holes, with the anterior electrode serving as the common channel and the other electrode as the channel 2 signal. Each electrode was connected to short tethered leads that mated with a 6-pin connector (Pinnacle Technologies) that was surgically affixed to the head of the animal using dental acrylic (Supplementary Fig. 11). This signal acquisition arrangement allowed us to collect bilateral EEG and perform a direct comparison of signal characteristics between the two electrodes using a within-animal approach (Supplementary Fig. 11).

Validation of wireless EEG against a tethered EEG system
These studies utilized nine 250–350 g Sprague Dawley rats from Charles River Laboratories. For each animal, three stainless-steel EEG screws (one common and two signal channels) were implanted into the skull and connected to short tethered leads that terminated in gold pins. The pins were mated to a 6-pin connector (P1 Technologies) that was surgically affixed to the head of the animal using dental acrylic. A custom bifurcated adapter split the EEG signals for simultaneous acquisition by a standard benchtop tethered EEG system (Neurosys) and the wireless device (graphically depicted in Supplementary Fig. 14). This approach gave each system access to signals originating from the

same EEG screws, allowing for precise temporal correlation of the wireless signal fidelity as compared to the gold-standard tethered system. Intraperitoneal injections of pharmaceuticals used the GABAB agonist baclofen (10 mg kg^{-1}) and the acetylcholinergic agonist pilocarpine (400 mg kg^{-1}, i.p.) dissolved in saline.

Wireless testing system
The full system setup included a tablet with a custom application for recording data and issuing commands wirelessly, a power distribution control (PDC) box, an antenna impedance-matching box, a laptop for controlling the output power level of the PDC box and a 31 cm × 34 cm × 31 cm (length × width × height) cage wired with a double-loop primary antenna. During testing, implanted rats moved freely and were fed ad libitum in the cage. The testing room was maintained on a 12 h light/dark cycle and climate controlled.

Acoustic setup and auditory stimuli
The auditory stimulation experiment used an acoustic startle sound attenuating chamber (Med Associates) that housed the aforementioned NFC wireless power transfer setup and the wired cage. An audio amplifier board (AMP2X15, PUI Audio) amplified sounds synthesized by MATLAB (MathWorks) and played the sounds through an exciter speaker (ASX03304-R, PUI Audio) mounted 30 cm above the animal. In situ acoustic calibration used a sound level meter (Protmex) placed on the floor of the cage. Background white noise created by a tone generator (Med Associates) at 60 dB was present throughout the experiment. Each stimulus set consisted of 10 short (100 ms) pure tones (5 kHz or 10 kHz) with inter-stimulus intervals pseudo-randomly varying between 5 s and 10 s. The data processing adopted ensemble averaging of EEG segments from the 10 trials in a stimulus set to attenuate the background EEG and enhance the signal-to-noise ratio.

Open-field test and motion tracking
The open-field test used a 31 cm × 34 cm × 31 cm (length × width × height) cage. Animals freely explored the open-field enclosure for 8 min under low-light conditions (50 lx). An overhead camera (5 MP wide angle USB camera OV5648, Arducam) recorded animal motion at 30 frames per second. Open Broadcaster Software (OBS) Studio 27.0.1 was used to record animal movement in mobility studies. Subsequent motion analysis utilized a deep learning model trained by DeepLabCut[51]. Manually marking 2 body parts (head and tail) in 1,000 representative frames generated a training set for a pre-trained CNN. Training the CNN for 100,000 epochs yielded the deep learning model that located the head and tail of the rat frame by frame. The corresponding trajectories of the head served as the basis for determining the head speed and total travel distance of the rats, as well as the travel distance and time spent in the outer zone and inner zone (defined as a square comprising the central 25% area of the cage).

Data collection and data analysis
Custom Python code with Python 3.8.10 and Bleak 0.12.1 was used to receive data by BLE. Custom Python code with Python 3.8.10, Scipy 1.7.3, Numpy 1.20.2, Pandas 1.2.5 and Matplotlib 3.3.4 was used to analyse EEG and EMG data and generate plots. Analysis of EEG and EMG data started with digital bandpass filtering using a Butterworth filter with a pass band of 0.5–40 Hz for EEG and 5–50 Hz for EMG. Spectral analysis used STFT with 2 s bins and 50% overlap. Corresponding spectrograms illustrated the time-frequency characteristics of each signal. Calculation of frequency spectra used the Welch's method. A linear Pearson correlation quantified the correlation between the spectra of the wireless and tethered systems.

Sleep–wake regulation data processing
The EEG spectrograms used power spectral density normalized by the total power across all frequencies at each bin to ensure a good

colour contrast agnostic to the absolute amplitudes of EEG across different stages of sleep. Two trained experts performed classification of sleep stages using a custom Python script that presented shuffled 30 s non-overlapping bins of synchronized EEG spectrograms and EMG time-series data for visual classification according to aforementioned criteria.

CNN model design, training and quantization

This demonstration used the CNN architecture, among other deep learning architectures, for a trade-off between accuracy and computation complexity. The CNN model started with a convolution layer with eight 7 × 7 filters to extract features of the spectrogram. A fully connected layer followed as a pattern matching layer, the output of which converted to a seizure score via softmax activation. The convolution and fully connected layers used ReLU activation for computation simplicity. The CNN model only had 12,002 parameters and 300,000 multiply-accumulate operations. The small CNN model achieved reasonably good accuracy for seizure and non-seizure classification in this demonstration. Therefore, more complex CNN models (as large as 150 kB after quantization) deployable on the same hardware, implemented for more complex classifications of seizure (ictal, preictal, interictal)[21], were not explored in this study. The training process used an ADAM optimizer and a random dataset split of 60%:20%:20% for training, validation and testing, with minimizing validation loss as the optimization criterion. Lastly, the TensorFlow Lite converter performed 8-bit quantization of the CNN model in a FlatBuffer format and a Unix tool named xxd converted the quantized model into a C array that could be compiled into the on-device programme, yielding a final model size of 14 kB.

On-device inference framework

The main function defines the setup() and loop() functions that are the core of the programme. The setup() function loads the quantized model and a subset of operations needed for the model (two-dimensional convolution, fully connected neural network and softmax activation) from the CMISS-NN library, builds an interpreter to run the model by passing the model and operations into the interpreter, and allocates a tensor arena of 10 kB for the model's tensors. Next, the loop() function is called again and again indefinitely to process continuously collected EEG data. The logic of the loop() function is as follows: (1) First, it checks whether new EEG data are available by the interrupt signal. The EEG AFE registers an interrupt signal once the first-in-first-out (FIFO) is full with a new batch of EEG points. The FIFO is capable of storing 32 EEG points (125 ms data at 256 Hz). (2) If new EEG data are available, the EEG Provider reads EEG data by SPI from the AFE and updates the array that stores the latest 3 s EEG data. (3) If new EEG data are provided by the EEG Provider, the Feature Provider function performs fast Fourier transform on the new EEG data via an open-source C++ library named kissfft and updates the spectrogram of the latest 3 s EEG[63]. (4) If 1.5 s pass since the last inference, the interpreter is invoked, which performs inference on the spectrogram and fills the output tensor with a seizure score. (5) If a new inference is performed, the Command Recognizer processes the latest seizure score, calculates the average score of the latest 30 s and determines whether a seizure is detected (average seizure score >128). (6) Finally, the Command Responder triggers drug delivery on the basis of the control policy.

Seizure studies using closed-loop drug delivery

Device-implanted animals were placed in an open-field cage enclosure for wireless EEG monitoring. Following 30 min of baseline recording, the animals were given an injection of scopolamine (1 mg kg^{-1}) subcutaneously to block peripheral muscarinic receptors. Approximately 15–30 min after that injection, the animals were given an intraperitoneal injection of pilocarpine (400 mg kg^{-1}) to induce seizure activity. A machine learning model was developed to automate seizure detection

on the basis of available datasets of pilocarpine-induced seizures and the code was installed on the device during manufacturing. Once the algorithm detected seizure activity, the wireless drug delivery system was activated to allow passive diffusion of midazolam (1 mg kg^{-1}) to stop seizure activity, or saline as a control. EEG signals were streamed in real time to a GUI for human monitoring, which, as a precautionary measure, supported override privileges for the researcher to trigger or not trigger the release of the therapeutic midazolam should the onboard seizure detection algorithm fail to trigger drug delivery correctly. Animals were continuously monitored throughout the studies and euthanized according to approved methods upon study conclusion.

Statistics and reproducibility

No statistical methods were used to predetermine sample sizes, but our sample sizes are similar to those reported in previous publications[10,12,13]. All samples were randomly assigned to experimental groups. Data from failed devices were excluded from the analysis. All data are expressed as mean ± s.e.m. or as individual plots. Data distribution was assumed to be normal, but this was not formally tested. For two-group comparisons, statistical significance was determined by two-tailed Student's *t*-tests.

Unless otherwise specified, each experiment was repeated 3 times independently with similar results.

Reporting summary

Further information on research design is available in the Nature Portfolio Reporting Summary linked to this article.

Data availability

The main data supporting the results in this study are available within the paper and its Supplementary Information. Source data for Figs. 2, 3, 4e–h and 6 are provided with this paper. Source data for Figs. 4i,j and 5 and the raw data are too large to be publicly shared, yet they are available for research purposes from the corresponding authors on reasonable request.

Code availability

The custom code for analysing electroencephalography and electromyography data is available at https://github.com/wouyanglv/Wireless_EEG.

References

1. Amiri, S., Fazel-Rezai, R. & Asadpour, V. A review of hybrid brain-computer interface systems. *Adv. Hum. Comput. Interact.* https://doi.org/10.1155/2013/187024 (2013).
2. Teplan, M. Fundamentals of EEG measurement. *Meas. Sci. Rev.* **2**, 1–11 (2002).
3. Tagluk, M. E., Sezgin, N. & Akin, M. Estimation of sleep stages by an artificial neural network employing EEG, EMG and EOG. *J. Med. Syst.* **34**, 717–725 (2010).
4. Won, S. M., Cai, L., Gutruf, P. & Rogers, J. A. Wireless and battery-free technologies for neuroengineering. *Nat. Biomed. Eng.* https://doi.org/10.1038/s41551-021-00683-3 (2021).
5. Srinivasan, N. Cognitive neuroscience of creativity: EEG based approaches. *Methods* **42**, 109–116 (2007).
6. Onton, J., Delorme, A. & Makeig, S. Frontal midline EEG dynamics during working memory. *Neuroimage* **27**, 341–356 (2005).
7. Mirowski, P., Madhavan, D., LeCun, Y. & Kuzniecky, R. Classification of patterns of EEG synchronization for seizure prediction. *Clin. Neurophysiol.* **120**, 1927–1940 (2009).
8. Eban-Rothschild, A., Appelbaum, L. & de Lecea, L. Neuronal mechanisms for sleep/wake regulation and modulatory drive. *Neuropsychopharmacology* **43**, 937–952 (2018).

9. Fuller, P. M., Gooley, J. J. & Saper, C. B. Neurobiology of the sleep-wake cycle: sleep architecture, circadian regulation, and regulatory feedback. *J. Biol. Rhythms* **21**, 482–493 (2006).

10. Yang, Y. et al. Wireless multilateral devices for optogenetic studies of individual and social behaviors. *Nat. Neurosci.* **24**, 1035–1045 (2021).

11. Zayachkivsky, A., Lehmkuhle, M. J. & Dudek, F. E. Long-term continuous EEG monitoring in small rodent models of human disease using the epoch wireless transmitter system. *J. Vis. Exp.* https://doi.org/10.3791/52554 (2015).

12. Park, S. et al. One-step optogenetics with multifunctional flexible polymer fibers. *Nat. Neurosci.* **20**, 612–619 (2017).

13. Jeong, J.-W. et al. Wireless optofluidic systems for programmable in vivo pharmacology and optogenetics. *Cell* **162**, 662–674 (2015).

14. Deisseroth, K. Optogenetics. *Nat. Methods* **8**, 26–29 (2011).

15. Chen, R., Canales, A. & Anikeeva, P. Neural recording and modulation technologies. *Nat. Rev. Mater.* https://doi.org/10.1038/natrevmats.2016.93 (2017).

16. Afshar, P. et al. A translational platform for prototyping closed-loop neuromodulation systems. *Front. Neural Circuits* **6**, 117 (2013).

17. Mirza, K. B., Golden, C. T., Nikolic, K. & Toumazou, C. Closed-loop implantable therapeutic neuromodulation systems based on neurochemical monitoring. *Front. Neurosci.* **13**, 808 (2019).

18. Roy, Y. et al. Deep learning-based electroencephalography analysis: a systematic review. *J. Neural Eng.* **16**, 51001 (2019).

19. Baldassano, S. et al. Cloud computing for seizure detection in implanted neural devices. *J. Neural Eng.* **16**, 26016 (2019).

20. Wang, F., Kaushal, R. & Khullar, D. Should health care demand interpretable artificial intelligence or accept "black box" medicine? *Ann. Intern. Med.* **172**, 59–60 (2020).

21. Liu, X. & Richardson, A. G. Edge deep learning for neural implants: a case study of seizure detection and prediction. *J. Neural Eng.* **18**, 46034 (2021).

22. Ahmad, I. et al. EEG-based epileptic seizure detection via machine/deep learning approaches: a systematic review. *Comput. Intell. Neurosci.* **2022**, 6486570 (2022).

23. Hügle, M. et al. Early seizure detection with an energy-efficient convolutional neural network on an implantable microcontroller. In *2018 International Joint Conference on Neural Networks (IJCNN)* 1–7 (IEEE, 2018).

24. Bahr, A. et al. Epileptic seizure detection on an ultra-low-power embedded RISC-V processor using a convolutional neural network. *Biosensors* **11**, 203 (2021).

25. David, R. et al. Tensorflow lite micro: embedded machine learning on tinyml systems. In *Proc. Machine Learning and Systems 3* (eds Smola, A., Dimakis, A. & Stoica, I.) 800–811 (MLSys, 2021).

26. Pinnell, R. C., Almajidy, R. K., Kirch, R. D., Cassel, J. C. & Hofmann, U. G. A wireless EEG recording method for rat use inside the water maze. *PLoS ONE* **11**, e0147730 (2016).

27. Jia, Y. et al. A software-defined radio receiver for wireless recording from freely behaving animals. *IEEE Trans. Biomed. Circuits Syst.* **13**, 1645–1654 (2019).

28. Zayachkivsky, A., Lehmkuhle, M. J., Fisher, J. H., Ekstrand, J. J. & Dudek, F. E. Recording EEG in immature rats with a novel miniature telemetry system. *J. Neurophysiol.* **109**, 900–911 (2013).

29. Chang, P., Hashemi, K. S. & Walker, M. C. A novel telemetry system for recording EEG in small animals. *J. Neurosci. Methods* **201**, 106–115 (2011).

30. Jung, Y. H. et al. Stretchable twisted-pair transmission lines for microwave frequency wearable electronics. *Adv. Funct. Mater.* **26**, 4635–4642 (2016).

31. Daniel, Ţ. D. & Neagu, M. in *Compendium of New Techniques in Harmonic Analysis* (ed. Lamchich, M. T.) Ch. 2 (IntechOpen, 2018).

32. Usakli, A. B. Improvement of EEG signal acquisition: an electrical aspect for state of the art of front end. *Comput. Intell. Neurosci.* **2010**, 630649 (2010).

33. Miladinović, Đ. et al. SPINDLE: end-to-end learning from EEG/EMG to extrapolate animal sleep scoring across experimental settings, labs and species. *PLoS Comput. Biol.* **15**, e1006968 (2019).

34. Tsimbalo, E., Fafoutis, X. & Piechocki, R. Fix it, don't bin it! - CRC error correction in Bluetooth low energy. In *2015 IEEE 2nd World Forum on Internet of Things (WF-IoT)* 286–290 (IEEE, 2015).

35. Wolf, P. D. in *Indwelling Neural Implants: Strategies for Contending with the In Vivo Environment* (ed. Reichert, W. M.) Ch. 3 (CRC Press/Taylor & Francis, 2008).

36. Kadam, S. D. et al. Methodological standards and interpretation of video-electroencephalography in adult control rodents. A TASK 1-WG 1 report of the AES/ILAE Translational Task Force of the ILAE. *Epilepsia* **58**, 10–27 (2017).

37. Gage, G. J. et al. Surgical implantation of chronic neural electrodes for recording single unit activity and electrocortico-graphic signals. *J. Vis. Exp.* https://doi.org/10.3791/3565 (2012).

38. Kim, R. & Nam, Y. Novel platinum black electroplating technique improving mechanical stability. In *2013 35th Annual International Conference of the IEEE Engineering in Medicine and Biology Society (EMBC)* 184–187 (IEEE, 2013).

39. Boyden, E. S., Zhang, F., Bamberg, E., Nagel, G. & Deisseroth, K. Millisecond-timescale, genetically targeted optical control of neural activity. *Nat. Neurosci.* **8**, 1263–1268 (2005).

40. Aravanis, A. M. et al. An optical neural interface: in vivo control of rodent motor cortex with integrated fiberoptic and optogenetic technology. *J. Neural Eng.* **4**, S143–S156 (2007).

41. Montgomery, K. L. et al. Wirelessly powered, fully internal optogenetics for brain, spinal and peripheral circuits in mice. *Nat. Methods* **12**, 969–974 (2015).

42. Zhang, Y. et al. Battery-free, fully implantable optofluidic cuff system for wireless optogenetic and pharmacological neuromodulation of peripheral nerves. *Sci. Adv.* **5**, eaaw5296 (2019).

43. Hodor, A., Palchykova, S., Gao, B. & Bassetti, C. L. Baclofen and gamma-hydroxybutyrate differentially altered behavior, EEG activity and sleep in rats. *Neuroscience* **284**, 18–28 (2015).

44. Sweeney-Reed, C. M., Nasuto, S. J., Vieira, M. F. & Andrade, A. O. Empirical mode decomposition and its extensions applied to EEG analysis: a review. *Adv. Data Sci. Adapt. Anal.* **10**, 1840001 (2018).

45. Budd, T. W. et al. Repetition suppression of the rat auditory evoked potential at brief stimulus intervals. *Brain Res.* **1498**, 59–68 (2013).

46. Nir, Y., Vyazovskiy, V. V., Cirelli, C., Banks, M. I. & Tononi, G. Auditory responses and stimulus-specific adaptation in rat auditory cortex are preserved across NREM and REM sleep. *Cereb. Cortex* **25**, 1362–1378 (2015).

47. Walsh, R. N. & Cummins, R. A. The open-field test: a critical review. *Psychol. Bull.* **83**, 482–504 (1976).

48. Díaz-Morán, S. et al. Relationships of open-field behaviour with anxiety in the elevated zero-maze test: focus on freezing and grooming. *World J. Neurosci.* https://doi.org/10.4236/wjns.2014.41001 (2014).

49. Sturman, O., Germain, P.-L. & Bohacek, J. Exploratory rearing: a context- and stress-sensitive behavior recorded in the open-field test. *Stress* **21**, 443–452 (2018).

50. Seibenhener, M. L. & Wooten, M. C. Use of the open field maze to measure locomotor and anxiety-like behavior in mice. *J. Vis. Exp.* https://doi.org/10.3791/52434 (2015).

51. Mathis, A. et al. DeepLabCut: markerless pose estimation of user-defined body parts with deep learning. *Nat. Neurosci.* **21**, 1281–1289 (2018).

52. Silva-Pérez, M., Sánchez-López, A., Pompa-del-Toro, N. & Escudero, M. Identification of the sleep–wake states in rats using the high-frequency activity of the electroencephalogram. *J. Sleep Res.* **30**, e13233 (2020).

53. Brankačk, J., Kukushka, V. I., Vyssotski, A. L. & Draguhn, A. EEG gamma frequency and sleep–wake scoring in mice: comparing two types of supervised classifiers. *Brain Res.* **1322**, 59–71 (2010).

54. Briese, E. Normal body temperature of rats: the setpoint controversy. *Neurosci. Biobehav. Rev.* **22**, 427–436 (1998).

55. Chen, M. C. et al. Anterior insula regulates multiscale temporal organization of sleep and wake activity. *J. Biol. Rhythms* **31**, 182–193 (2016).

56. Machado, R. B., Tufik, S. & Suchecki, D. Role of corticosterone on sleep homeostasis induced by REM sleep deprivation in rats. *PLoS ONE* **8**, e63520 (2013).

57. Zhang, H. et al. Wireless, battery-free optoelectronic systems as subdermal implants for local tissue oximetry. *Sci. Adv.* **5**, eaaw0873 (2019).

58. Kim, S. et al. Soft, skin-interfaced microfluidic systems with integrated immunoassays, fluorometric sensors, and impedance measurement capabilities. *Proc. Natl Acad. Sci. USA* **117**, 27906–27915 (2020).

59. Burton, A. et al. Wireless, battery-free, and fully implantable electrical neurostimulation in freely moving rodents. *Microsyst. Nanoeng.* https://doi.org/10.1038/s41378-021-00294-7 (2021).

60. Mickle, A. D. et al. A wireless closed-loop system for optogenetic peripheral neuromodulation. *Nature* **565**, 361–365 (2019).

61. Lee, K. H. et al. Mechano-acoustic sensing of physiological processes and body motions via a soft wireless device placed at the suprasternal notch. *Nat. Biomed. Eng.* **4**, 148–158 (2020).

62. Won, S. M., Song, E., Reeder, J. T. & Rogers, J. A. Emerging modalities and implantable technologies for neuromodulation. *Cell* **181**, 115–135 (2020).

63. Borgerding, M. kissfft (GitHub, 2022); https://github.com/mborgerding/kissfft

Additional information

Extended data is available for this paper at https://doi.org/10.1038/s41551-023-01029-x.

Supplementary information The online version contains supplementary material available at https://doi.org/10.1038/s41551-023-01029-x.

Correspondence and requests for materials should be addressed to Thomas C. Jhou, Cameron H. Good or John A. Rogers.

Peer review information *Nature Biomedical Engineering* thanks Max Ortiz-Catalan, Silvestro Micera and Thomas Stieglitz for their contribution to the peer review of this work.

**Reprints and permissions information** is available at www.nature.com/reprints.

¹Querrey Simpson Institute for Bioelectronics, Northwestern University, Evanston, IL, USA. ²Department of Electrical and Computer Engineering, Northwestern University, Evanston, IL, USA. ³School of Chemical Engineering, Sungkyunkwan University, Suwon, Republic of Korea. ⁴Department of Materials Science and Engineering, Northwestern University, Evanston, IL, USA. ⁵Neurolux Inc., Northfield, IL, USA. ⁶Department of Mechanical Engineering, Northwestern University, Evanston, IL, USA. ⁷US Army Research Laboratory, Aberdeen Proving Ground, MD, USA. ⁸US Army Medical Research Institute of Chemical Defense, Aberdeen Proving Ground, MD, USA. ⁹SURVICE Engineering, Belcamp, MD, USA. ¹⁰Department of Civil and Environmental Engineering, Northwestern University, Evanston, IL, USA. ¹¹Department of Electrical and Computer Engineering, Sungkyunkwan University, Suwon,

Republic of Korea. [12]School of Electrical Engineering, Korea Advanced Institute of Science and Technology, Daejeon, Republic of Korea. [13]Department of Applied Physical Sciences, University of North Carolina at Chapel Hill, Chapel Hill, NC, USA. [14]Department of Biomedical Engineering, Northwestern University, Evanston, IL, USA. [15]Department of Chemical and Biological Engineering, Northwestern University, Evanston, IL, USA. [16]Department of Chemistry, Northwestern University, Evanston, IL, USA. [17]Developmental Therapeutics Core, Northwestern University, Evanston, IL, USA. [18]Center for Advanced Molecular Imaging, Northwestern University, Evanston, IL, USA. [19]Biomedical Institute for Convergence at SKKU (BICS), Sungkyunkwan University (SKKU), Suwon, Republic of Korea. [20]Department of Neurosciences, Medical University of South Carolina, Charleston, SC, USA. [21]Department of Neurological Surgery, Feinberg School of Medicine, Northwestern University, Evanston, IL, USA. [22]These authors contributed equally: Wei Ouyang, Wei Lu, Yamin Zhang. ✉e-mail: jhou@musc.edu; cameron.good@northwestern.edu; jrogers@northwestern.edu
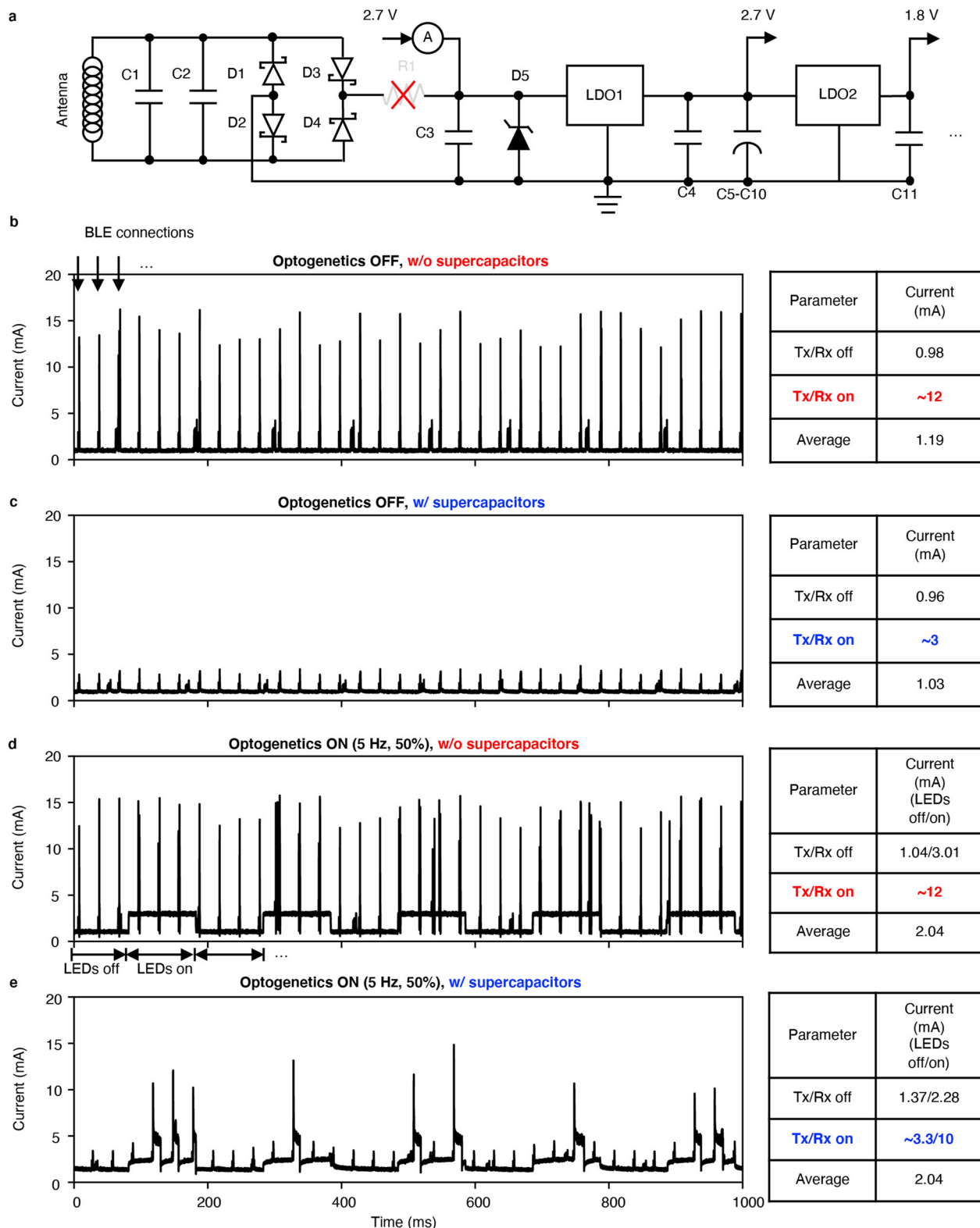
Extended Data Fig. 1 | Power consumption profiles of the device under different configurations. a, Testing scheme in which a sourcemeter is used as a power source instead of the NFC power. (**b, c**) Power profiles with the optogenetics module inactivated (b) without and (c) with supercapacitors. The supercapacitors effectively mitigate the power surges during BLE data transceiving (Tx/Rx). The tables summarize the current consumption in different operating stages. (**d, e**) Power profiles with the optogenetics module activated (d) without and (e) with supercapacitors. The supercapacitors mitigate power surges during active LEDs and active BLE Rx/Tx and are recharged during lower power consumptions. The tables summarize the current consumption in different operating stages.
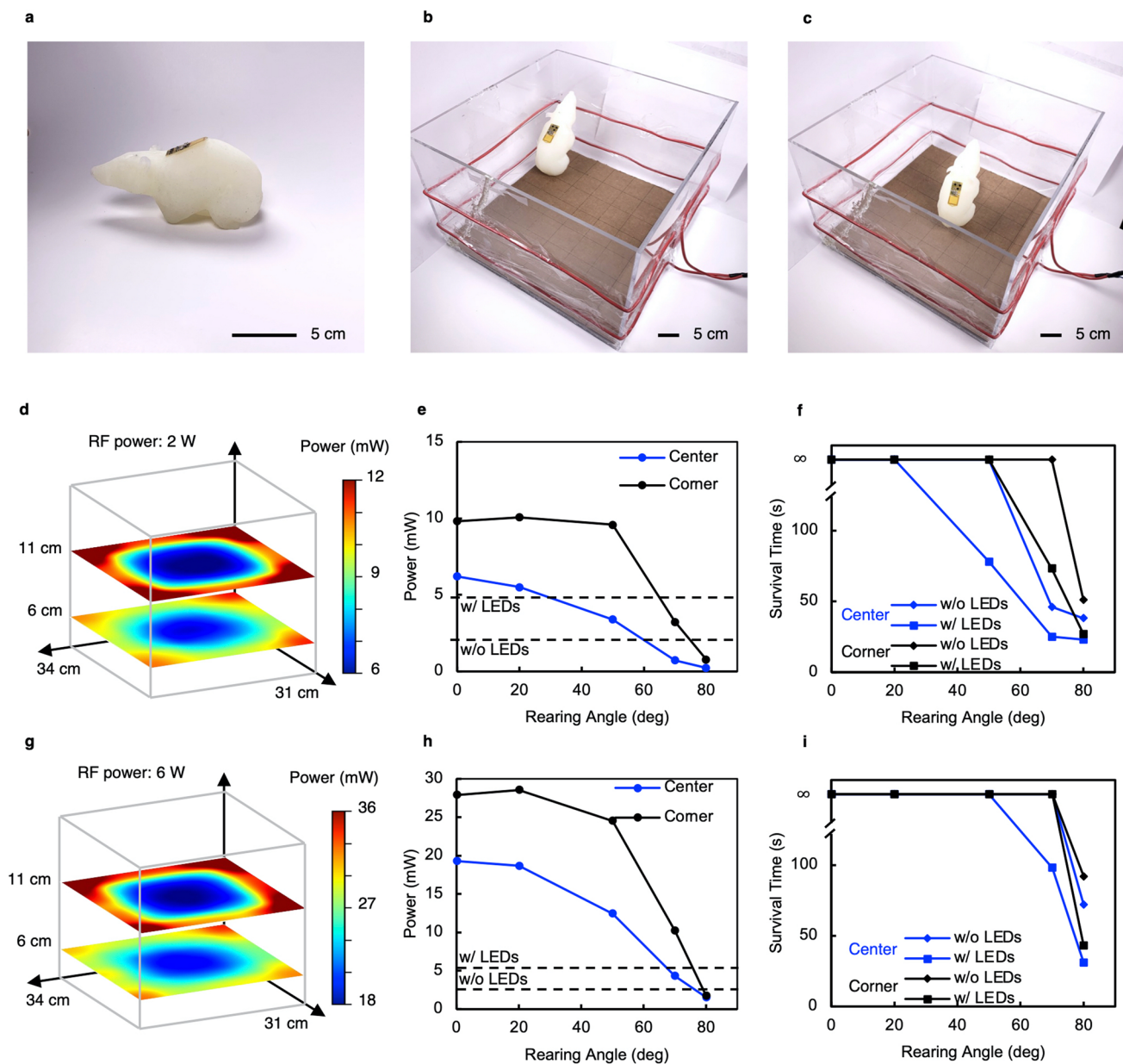
Extended Data Fig. 2 | Characterization of the wireless power transfer performance. a, A device mounted on an agarose gel rat model for measuring the effect of rat rearing angle on the wireless power transfer and device survival time. **b**, Experiment setup simulating the rearing of a rat at the corner of the cage. **c**, Experiment setup simulating the rearing of a rat at the center of the cage. **d**, The power received by the device at different heights and locations of the cage under an input RF power of 2 W. **e**, The power received by the device when the rat rears with different angles at the center and corner of the cage under an input RF power of 2 W. **f**, Device survival time (that is device working time before it loses power to support its operation) at different rat rearing angles. The device is started normally and then the rat holds a rearing angle for an extended period of time at the center and corner of the cage under an input RF power of 2 W. **g**, The power received by the device at different heights and locations of the cage under an input RF power of 6 W. **h**, The power received by the device when the rat rears with different angles at the center and corner of the cage under an input RF power of 6 W. **i**, Device survival time at different rat rearing angles under an input RF power of 6 W.
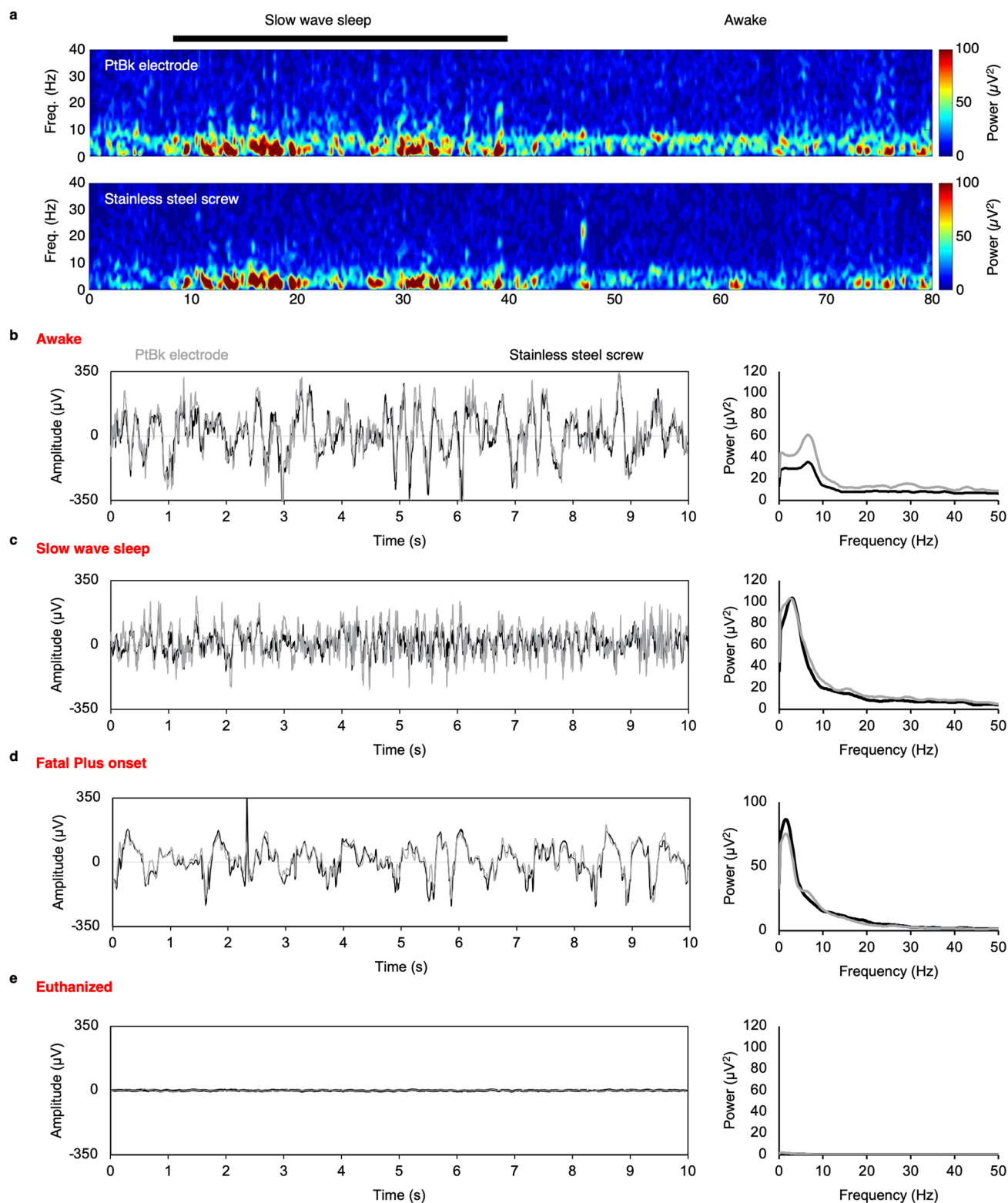
Extended Data Fig. 3 | Acute in vivo comparison of EEG signals measured by the PtBk-plated EEG electrodes and stainless steel screws. a, EEG spectrograms during slow wave sleep and awake states in a rat show good correlation between the PtBk-plated EEG electrodes and stainless steel screws. (**b-e**) Comparison of time-domain EEG signals (left) and EEG power spectra (right) measured by of the PtBk-plated EEG electrodes and stainless steel screws during (b) awake, (c) slow wave sleep, (d) fatal plus onset, and (e) euthanized states and their correlations.
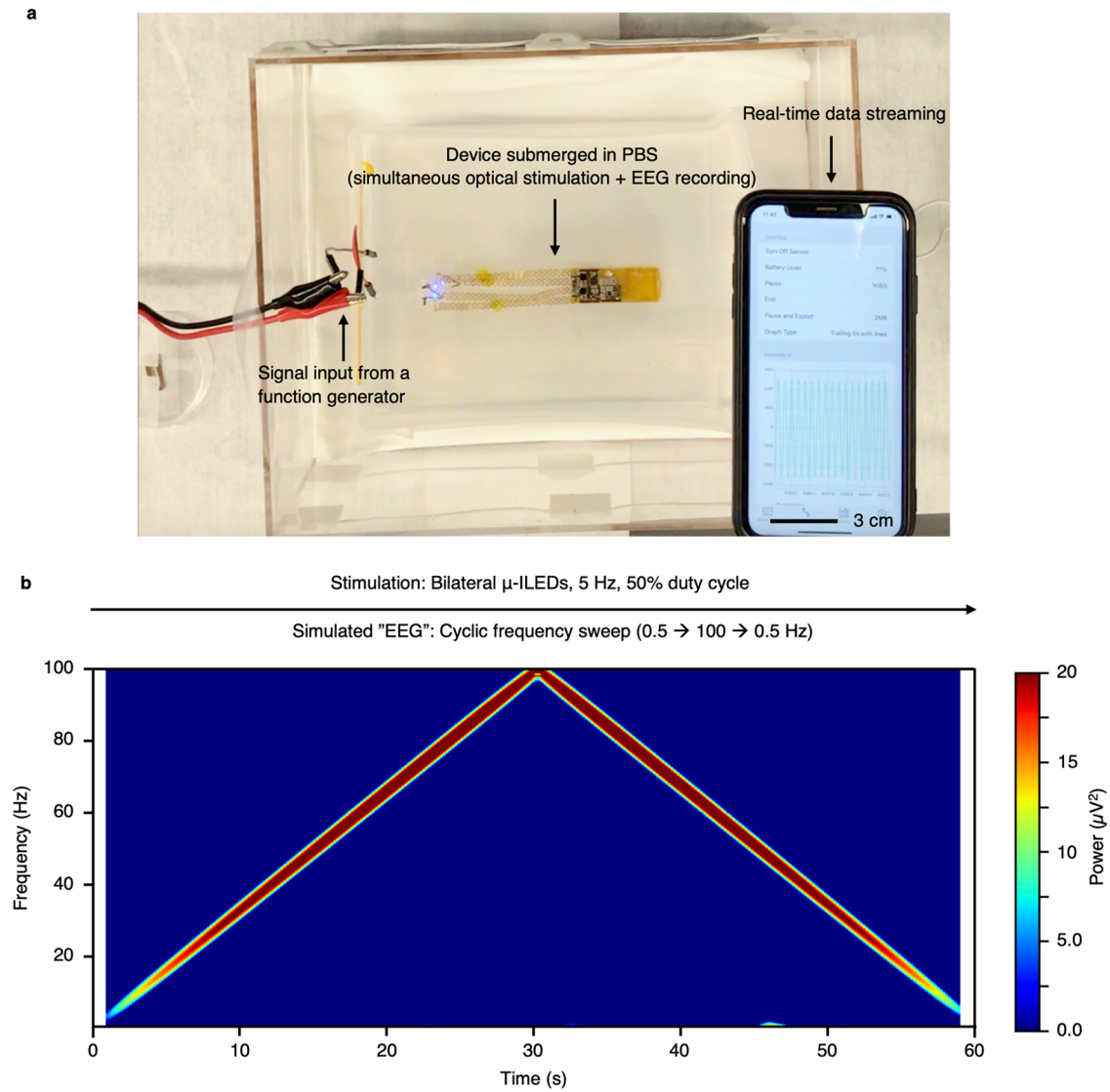
Extended Data Fig. 4 | Benchtop validation of simultaneous optogenetic stimulation and electrical recording in PBS. a, Experimental setup in which the device was submerged in PBS to simulate the electrical conduction of the body of a rat. The device performed simultaneous bilateral optical stimulation at 5 Hz (50% duty cycle) and electrical recording. The electrical signal was fed through PBS by a function generator that performed a cyclic frequency sweep (0.5 → 100 → 0.5 Hz) with a constant amplitude. **b**, Spectrogram showing recorded signal from the test. The signal showed clean frequency characteristics without interference from the μ-ILEDs, which would show as a horizontal band at 5 Hz if it existed. The video recording of the experiment is provided as Supplementary Video 1.
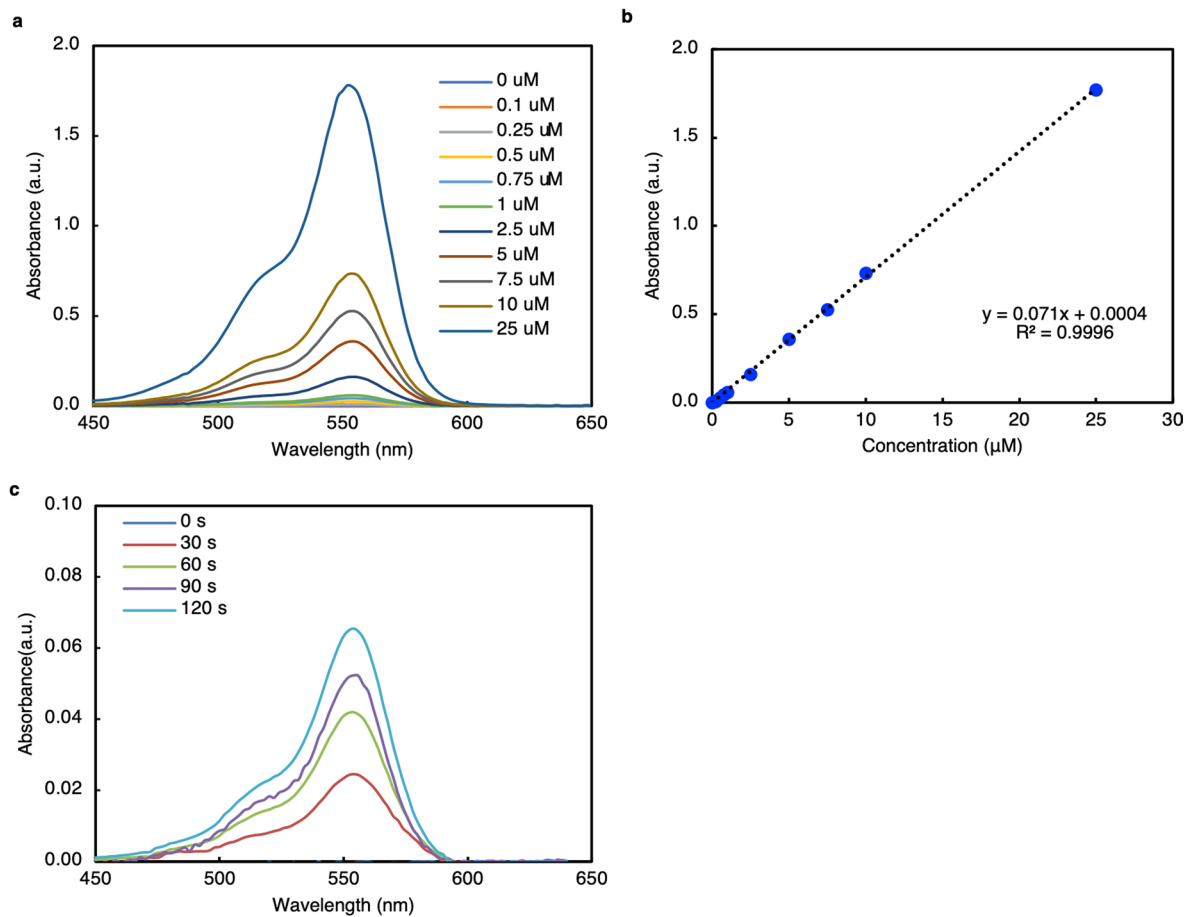
Extended Data Fig. 5 | Characterization of drug-release rate. a, UV-Vis spectra of different concentrations of Rhodamine B. **b**, Calibration curve of absorption at 550 nm v.s. concentration of Rhodamine B. **c**, UV-Vis spectra of PBS containing Rhodamine B released from the drug delivery vehicle at different time since electrolysis was triggered.
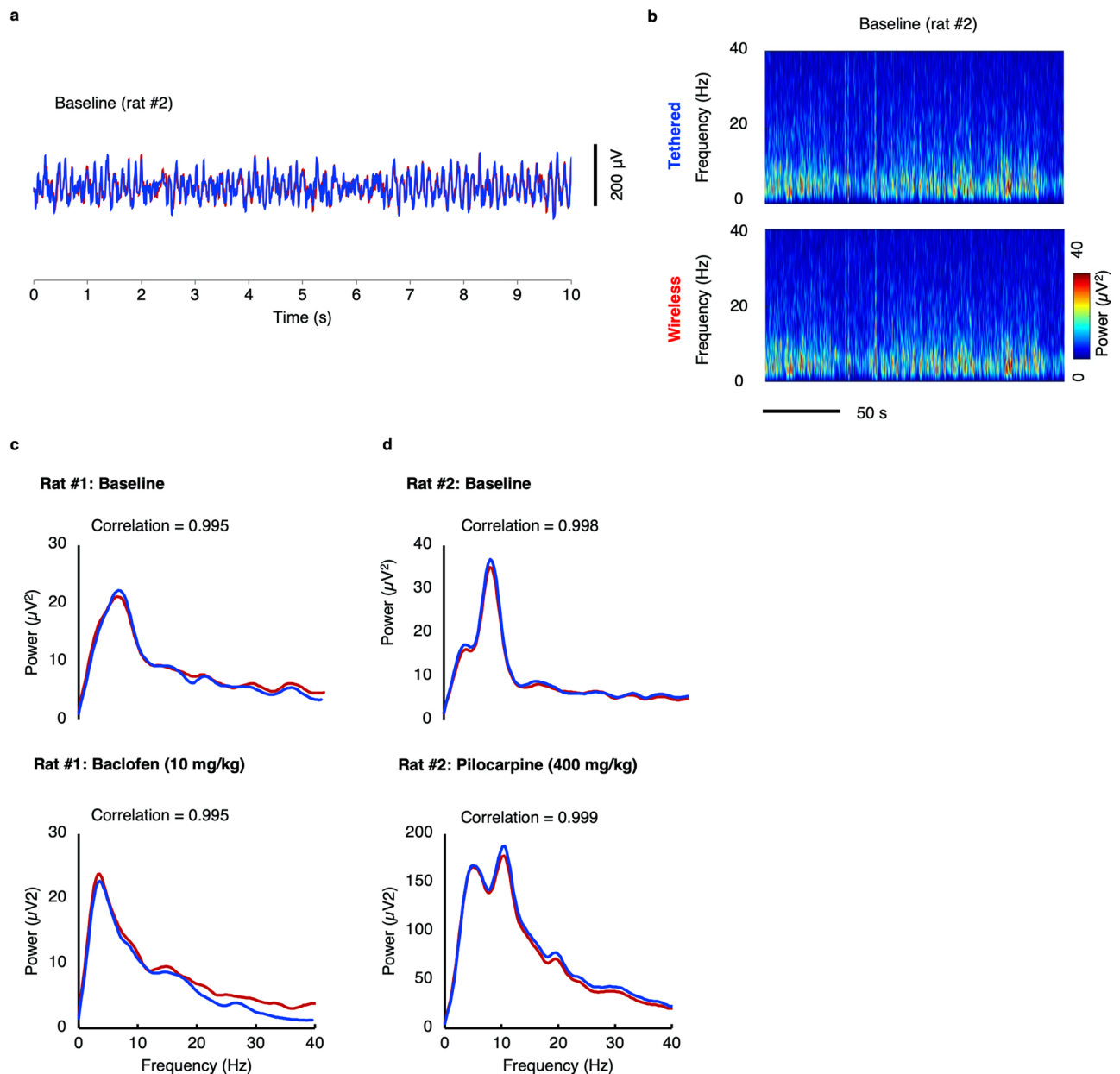
Extended Data Fig. 6 | Additional data on validating the wireless EEG system against the conventional tethered system. a, Baseline time-domain EEG data of rat #2 (used for pilocarpine stimulation study). **b**, Spectrograms of the baseline EEG of rat #2 measured by the tethered and wireless systems, respectively. **c**, The frequency spectra of EEG data measured by the tethered and wireless systems at the baseline and after baclofen stimulation. **d**, The frequency spectra of EEG data measured by the tethered and wireless systems at the baseline and after pilocarpine stimulation.
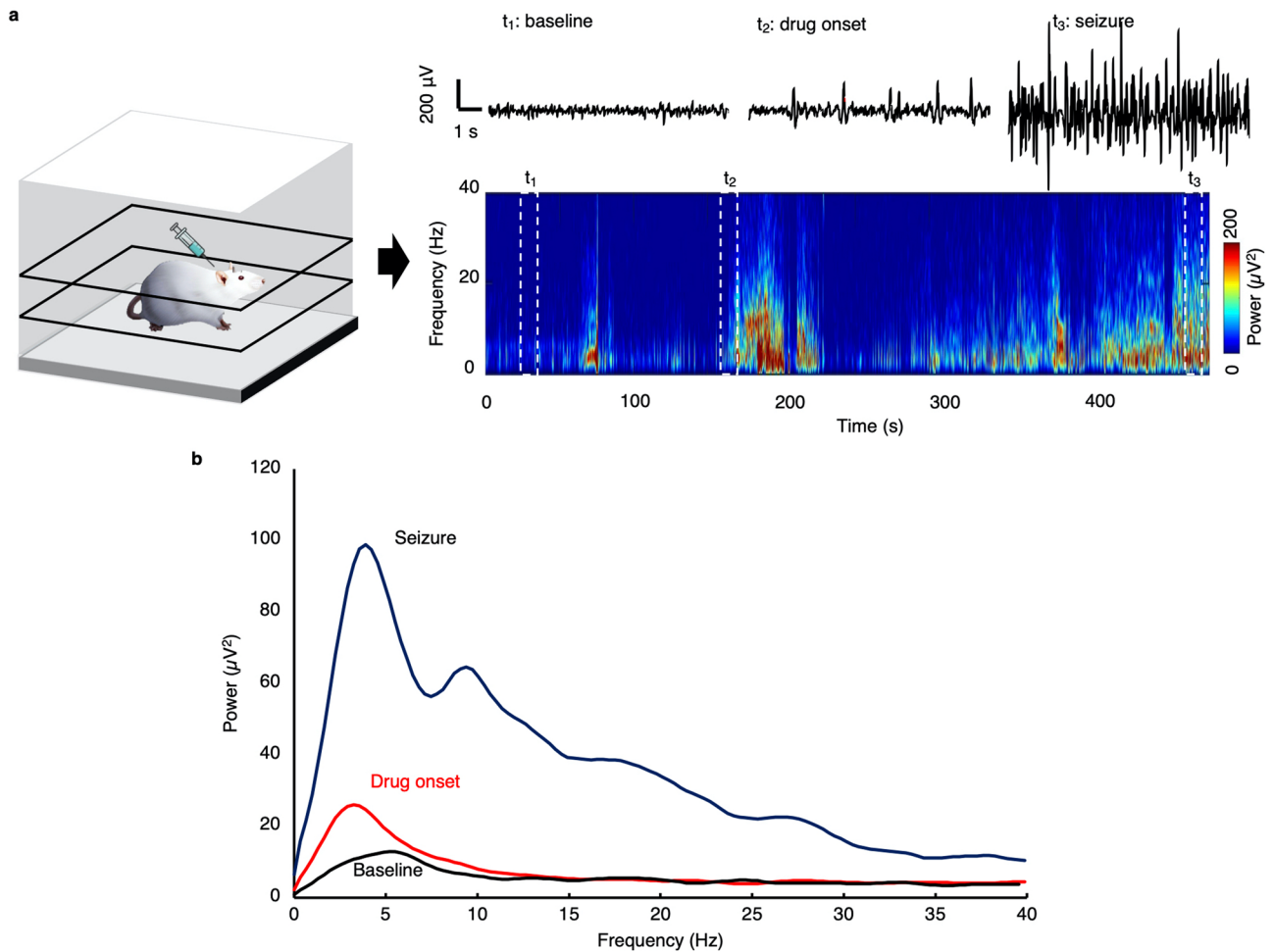
Extended Data Fig. 7 | Validation of the wireless neurorecording functionality in its final intended, fully implanted configuration using the pilocarpine-induced seizure model. a, EEG data measured by a fully implanted device in a rat under the stimulation of Pilocarpine (400 mg/kg). **b**, The corresponding frequency spectra of EEG at different conditions (baseline, drug onset, and seizure).
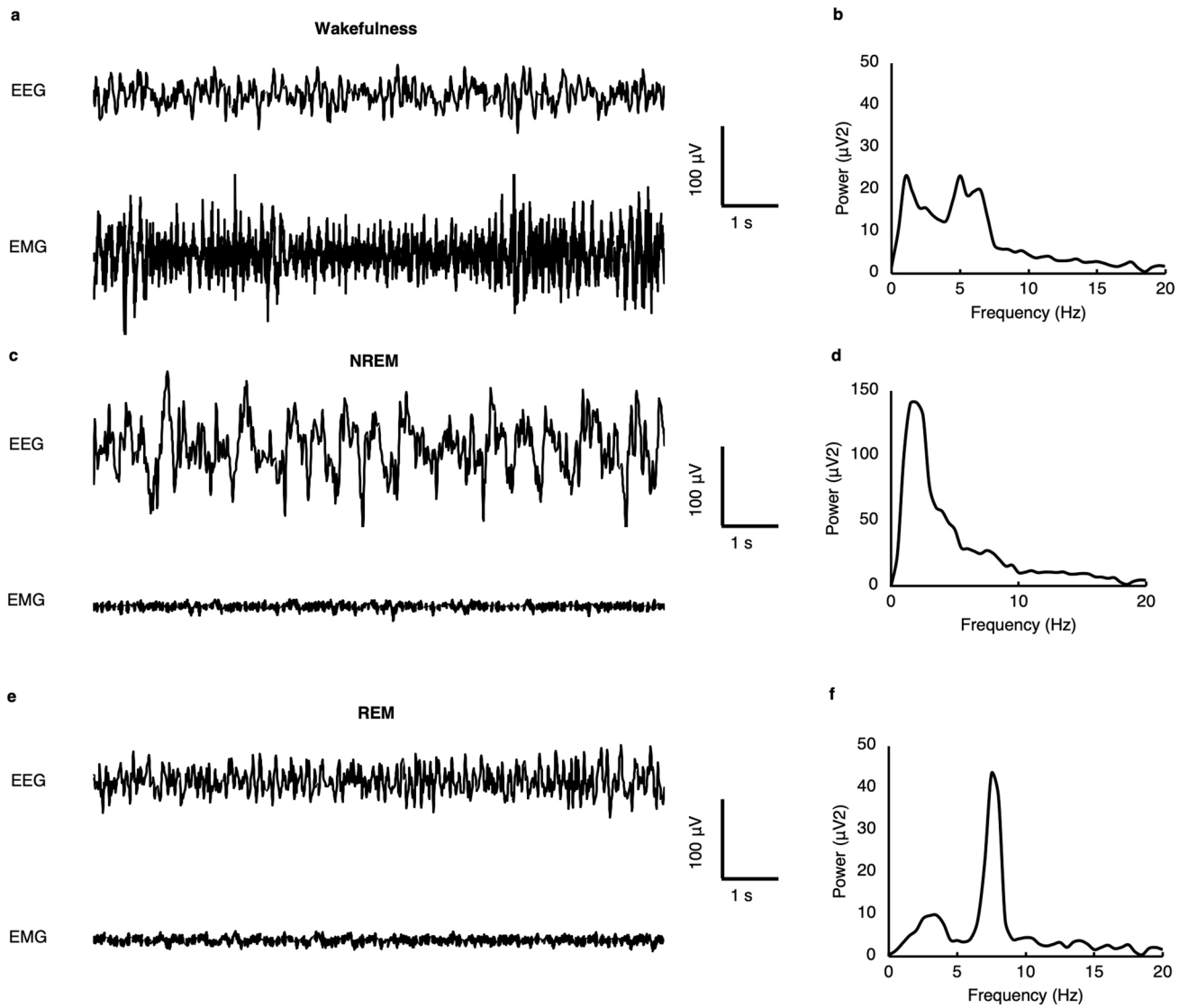
Extended Data Fig. 8 | Characteristics of different sleep stages measured by the fully implanted, wireless device. a, Time-domain data of EEG and EMG during wakefulness. **b**, Power spectrum of EEG during wakefulness showing medium powers in the delta band (0.5–4 Hz) and theta band (6–9 Hz). **c**, Time-domain data of EEG and EMG during NREM sleep. **d**, Power spectrum of EEG during NREM sleep showing a high power in the delta band (0.5–4 Hz) and a low power in the theta band (6–9 Hz). **e**, Time-domain data of EEG and EMG during REM sleep. **f**, Power spectrum of EEG during REM sleep showing a low power in the delta band (0.5–4 Hz) and a high power in the theta band (6–9 Hz).
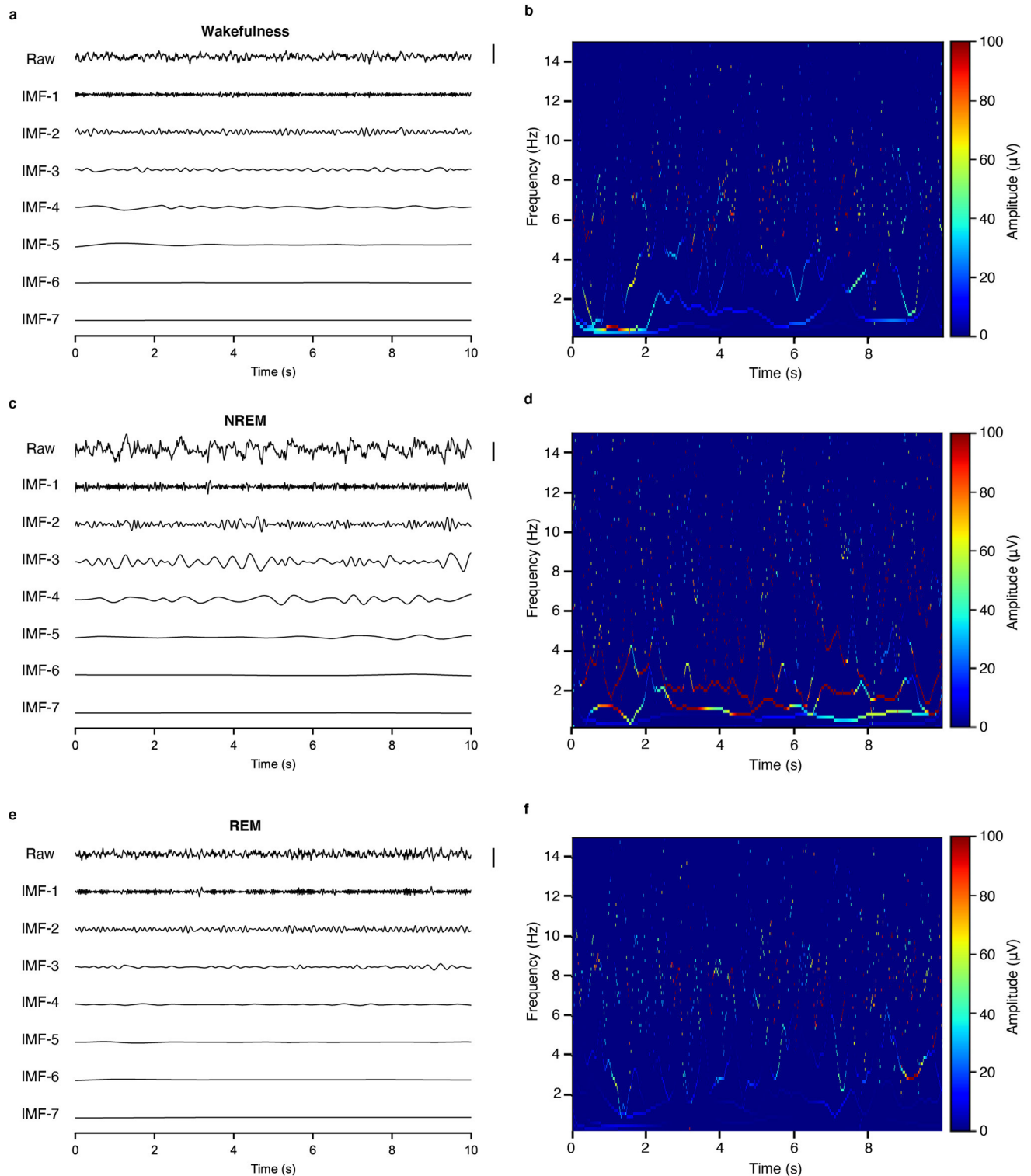
Extended Data Fig. 9 | Empirical mode decomposition of representative signals at different sleep stages. a, EMD of EEG during wakefulness. **b**, Hilbert-Huang transform of EMD during wakefulness. **c**, EMD of EEG during NREM. **d**, Hilbert-Huang transform of EMD during NREM. **e**, EMD of EEG during rem. **f**, Hilbert-Huang transform of EMD during REM. The scale bar represents 100 μV.
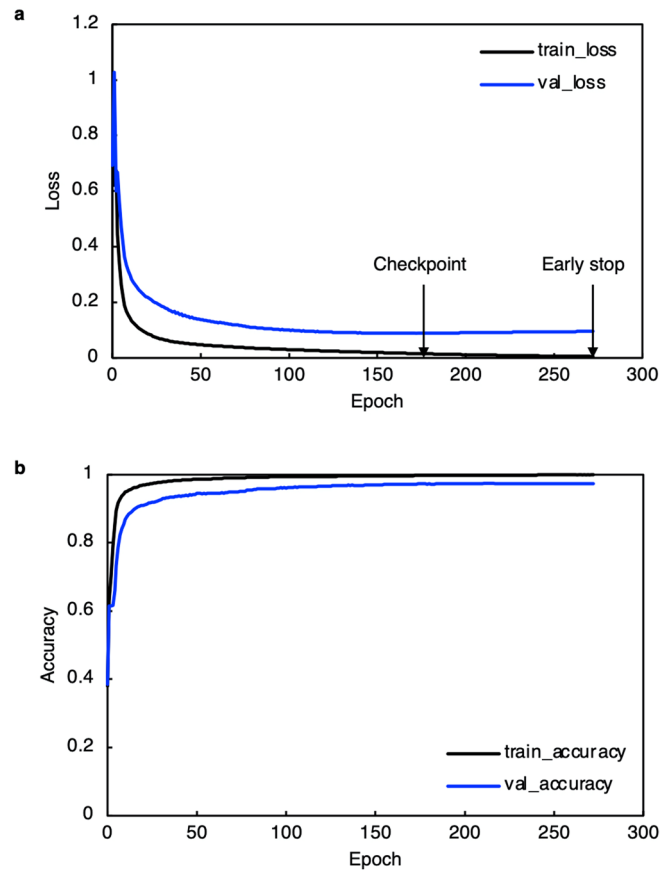
Extended Data Fig. 10 | Metrics of training the CNN model. a, Training and validation loss. **b**, Training and validation accuracy.

nature portfolio

Corresponding author(s):	Thomas C. Jhou, Cameron H. Good and John A. Rogers
Last updated by author(s):	Mar 24, 2023

Reporting Summary

Nature Portfolio wishes to improve the reproducibility of the work that we publish. This form provides structure for consistency and transparency in reporting. For further information on Nature Portfolio policies, see our Editorial Policies and the Editorial Policy Checklist.

Statistics

For all statistical analyses, confirm that the following items are present in the figure legend, table legend, main text, or Methods section.

n/a	Confirmed	
☐	☒	The exact sample size (*n*) for each experimental group/condition, given as a discrete number and unit of measurement
☐	☒	A statement on whether measurements were taken from distinct samples or whether the same sample was measured repeatedly
☐	☒	The statistical test(s) used AND whether they are one- or two-sided *Only common tests should be described solely by name; describe more complex techniques in the Methods section.*
☐	☒	A description of all covariates tested
☐	☒	A description of any assumptions or corrections, such as tests of normality and adjustment for multiple comparisons
☐	☒	A full description of the statistical parameters including central tendency (e.g. means) or other basic estimates (e.g. regression coefficient) AND variation (e.g. standard deviation) or associated estimates of uncertainty (e.g. confidence intervals)
☐	☒	For null hypothesis testing, the test statistic (e.g. F, t, r) with confidence intervals, effect sizes, degrees of freedom and P value noted *Give P values as exact values whenever suitable.*
☒	☐	For Bayesian analysis, information on the choice of priors and Markov chain Monte Carlo settings
☒	☐	For hierarchical and complex designs, identification of the appropriate level for tests and full reporting of outcomes
☒	☐	Estimates of effect sizes (e.g. Cohen's *d*, Pearson's *r*), indicating how they were calculated

Our web collection on statistics for biologists contains articles on many of the points above.

Software and code

Policy information about availability of computer code

Data collection	Custom Python code with Python 3.8.10 and Bleak 0.12.1 was used to receive data by bluetooth-low-energy. ABAQUS (ABAQUS Analysis User's 554 Manual 2016) was used for mechanical simulation. OceanView 2.0.7 was used to collect optical-light intensity. Open Broadcaster Software (OBS) Studio 27.0.1 was used to record animal movement in mobility studies.
Data analysis	Custom Python code with Python 3.8.10, Scipy 1.7.3, Numpy 1.20.2, Pandas 1.2.5, Matplotlib 3.3.4 was used to analyse electroencephalography and electromyography data and to generate plots (https://github.com/wouyanglv/Wireless_EEG). Statistical analyses were performed using GraphPad Prism 7 software (GraphPad, LaJolla, CA). Animal movement traces were analysed by custom code with DeepLabCut 2.2.0.2 and Python 3.8.11. MicroCT imaging data were analysed with Amira v2020.2.

For manuscripts utilizing custom algorithms or software that are central to the research but not yet described in published literature, software must be made available to editors and reviewers. We strongly encourage code deposition in a community repository (e.g. GitHub). See the Nature Portfolio guidelines for submitting code & software for further information.

Data

Policy information about availability of data

All manuscripts must include a data availability statement. This statement should provide the following information, where applicable:
- Accession codes, unique identifiers, or web links for publicly available datasets
- A description of any restrictions on data availability
- For clinical datasets or third party data, please ensure that the statement adheres to our policy

> The main data supporting the results in this study are available within the paper and its Supplementary Information. Source data for Figs. 2, 3, 4e-h, and 6 are provided with this paper. Source data for Figs. 4i-j and Fig. 5 and the raw data are too large to be publicly shared, yet they are available for research purposes from the corresponding authors on reasonable request.

Human research participants

Policy information about studies involving human research participants and Sex and Gender in Research.

Reporting on sex and gender	The study did not involve human research participants.
Population characteristics	—
Recruitment	—
Ethics oversight	—

Note that full information on the approval of the study protocol must also be provided in the manuscript.

Field-specific reporting

Please select the one below that is the best fit for your research. If you are not sure, read the appropriate sections before making your selection.

☒ Life sciences   ☐ Behavioural & social sciences   ☐ Ecological, evolutionary & environmental sciences

For a reference copy of the document with all sections, see nature.com/documents/nr-reporting-summary-flat.pdf

Life sciences study design

All studies must disclose on these points even when the disclosure is negative.

Sample size	Required sample sizes were estimated on the basis of previous reports of published results and of our past experience performing similar experiments. No statistical methods were used to predetermine sample sizes, but our sample sizes are similar to those reported in previous publications (Y. Yang, Nat. Neurosci. 24, 1035–1045 (2021); G. Shin, Neuron 93, 509–521 (2017)).
Data exclusions	Data from failed devices were excluded from analysis.
Replication	All experiments were repeated at least twice. All attempts at replication were successful.
Randomization	The animals were randomly assigned to experimental groups.
Blinding	The investigators were blinded to group assignment during data collection and data analysis.

Reporting for specific materials, systems and methods

We require information from authors about some types of materials, experimental systems and methods used in many studies. Here, indicate whether each material, system or method listed is relevant to your study. If you are not sure if a list item applies to your research, read the appropriate section before selecting a response.

Materials & experimental systems

n/a	Involved in the study
☒	☐ Antibodies
☒	☐ Eukaryotic cell lines
☒	☐ Palaeontology and archaeology
☐	☒ Animals and other organisms
☒	☐ Clinical data
☒	☐ Dual use research of concern

Methods

n/a	Involved in the study
☒	☐ ChIP-seq
☒	☐ Flow cytometry
☒	☐ MRI-based neuroimaging

Animals and other research organisms

Policy information about studies involving animals; ARRIVE guidelines recommended for reporting animal research, and Sex and Gender in Research

Laboratory animals	Adult Sprague-Dawley rats (250–350 g, 8–12 weeks old at the start of the experiments) from Charles River Laboratories (Wilmington, MA) were used in all animal experiments.
Wild animals	The study did not involve wild animals.
Reporting on sex	The findings apply equally to both sexes (forty-four Sprague-Dawley rats were used, 9 female). No sex-based analyses were performed, because the device is agnostic to signal inputs and both sexes have comparable physiological responses.
Field-collected samples	The study did not involve samples collected from the field.
Ethics oversight	All experimental procedures were approved by the Institutional Animal Care and Use Committee (IACUC) of Northwestern University or of the Medical University of South Carolina.

Note that full information on the approval of the study protocol must also be provided in the manuscript.